

Bulge-Disk Decompositions and Structural Bimodality of Ursa Major Cluster Spiral Galaxies

Michael McDonald^{1,*}, Stéphane Courteau¹, & R. Brent Tully²

¹*Department of Physics, Engineering Physics and Astronomy, Queen’s University, Kingston, ON, Canada*

^{*}*Currently at University of Maryland, College Park, MD*

²*Institute for Astronomy, University of Hawaii, 2680 Woodlawn Drive, Honolulu, HI*

mcdonald@astro.umd.edu, courteau@astro.queensu.ca, tully@ifa.hawaii.edu

30 May 2018

ABSTRACT

We present bulge and disk (B/D) decompositions of existing K' surface brightness profiles for 65 Ursa Major cluster spiral galaxies. This improves upon the disk-only fits of Tully et al. (1996). The 1996 disk fits were used by Tully & Verheijen (1997) for their discovery of the bimodality of structural parameters in the UMa cluster galaxies. It is shown that our new 1D B/D decompositions yield disk structural parameters that differ only slightly from the basic fits of Tully et al. and evidence for structural bimodality of UMa galaxies is maintained. Our B/D software for the decomposition of 1D surface brightness profiles of galaxies uses a non-linear minimization scheme to recover the best fitting Sérsic bulge and exponential disk while accounting for the possible presence of a compact nucleus and spiral arms and for the effects of seeing and disk truncations. In agreement with Tully & Verheijen, we find that the distribution of near-infrared disk central surface brightnesses is bimodal with an F-test confidence of 80%. There is also strong evidence for a local minimum in the luminosity function at $M_{K'} \simeq -22$. A connection between the brightness bimodality and a dynamical bimodality, based on new HI line widths, is identified. The B/D parameters are presented in an Appendix.

1 INTRODUCTION

The discovery of structural bimodality of Ursa Major (hereafter UMa) cluster galaxies by Tully & Verheijen (1997; hereafter TV97) remains of tremendous interest in light of its implications for galaxy formation models and the fact that it still lacks, a full decade later, a firm theoretical explanation. Tully et al. (1996; hereafter T96) reported deep multiband BRI and K' imaging of a complete sample of 65 UMa cluster galaxies. The analysis of these data by TV97 revealed a striking bimodality in the distribution of inclination-corrected disk central surface brightnesses, μ_0^i . Rather than showing a monotonic range of values starting at the Freeman peak¹ for brightest galaxies, the distribution of μ_0^i found by TV97 showed two distinct peaks describing low surface brightness (hereafter LSB) galaxies and high surface brightness (hereafter HSB) galaxies respectively. Using the deep IR imaging alone, which is largely insensitive to dust extinction, TV97 found that UMa spiral galaxies seem to avoid disk central surface brightnesses around $\mu_{0,K} \simeq 18.5$ mag arcsec⁻².

T96 fitted exponential disks to the light profiles of the

65 UMa galaxies. These fits yield a value for μ_0 and the disk scale length, h . The inclination correction for μ_0 used by TV97 included both geometric and extinction terms, as follows:

$$\mu_0^i = \mu_0 - 2.5C^\lambda \log(b/a) \quad (1)$$

where C^λ is the wavelength-dependent extinction correction term and b/a is the axial ratio. For NIR imaging, and LSB galaxies at all wavelengths, it was assumed that $C^\lambda = 1$; other values for C^λ at other dust-sensitive wavelengths for HSB galaxies were used by TV97. At K' , the distribution of inclination-corrected μ_0^i shows two distinct peaks at 17.3 K' mag arcsec⁻² for HSB galaxies and 19.7 K' mag arcsec⁻² for LSB galaxies. The bimodality of the μ_0 distribution was not convincingly observed at optical (BRI) bands but correcting the optical surface brightness profiles for inclination and extinction effects reveals a surface brightness bimodality in these bands as well. TV97 stressed it could not be excluded that the SB bimodality at optical bands is an artifact of their extinction correction which applies to HSB galaxies alone. Nonetheless, the fact that the K' -band is mostly insensitive to dust and that the distribution of $\mu_{0,K}^i$ is strongly bimodal is sufficient ground for TV97’s case of structural bimodality in spiral galaxies.

TV97 also considered possible environment dependences of the distribution of μ_0^i such as effects due to the

¹ Freeman (1970) found a very narrow peak in the distribution of disk central surface brightnesses at $\mu_0^B = 21.65$ for a sample of 28 bright spiral and lenticular galaxies.

stripping of gas and stars. They divided their sample into galaxies with and without a significant near-neighbour and found, despite the statistical limitations, evidence for an enhancement of the bimodality in the more isolated galaxies (see TV97 for details). Most galaxies with intermediate μ_0^i values were found to have near significant neighbours.

Various sources of bias in TV97's analysis should however be considered before its results can be fully embraced. These include the small size of the UMa cluster sample (Bell & de Blok 2000), the fact that the tentative findings may be particular to the UMa cluster (which contains mostly HI -rich spirals), the need for an independent analysis of the data, and the unaccounted contribution of the bulge to the disk fits. The first two issues (small-number statistics and UMa-centric analysis) can be addressed by repeating TV97's analysis with a larger sample that encompasses the full range of Hubble types. We report such an analysis for 297 Virgo cluster galaxies in McDonald et al. (2008).

The need for an independent analysis and the study of the bulge contribution to the disk scale lengths used by TV97 to infer the bimodal distribution of μ_0 will be addressed simultaneously in this paper. TV97 obtained μ_0 from exponential fits that avoided the bulge component. The uncertainty in this "marking-the-disk" technique depends on the subjective interpretation of the bulge size and the disk fit baseline. For large bulges, a shorter inner fit boundary would bias the disk μ_0 high. The presence of smaller bulges should not affect the measurement of μ_0 .

Below, we discuss our own derivation of surface brightness profiles from the original deep K' -band images from T96 using our own isophotal fitting software. We then decomposed the new profiles using our 1D B/D decomposition program. The measurement of μ_0 by T96 relied on the inward extrapolation of an exponential function fitted to the galaxy surface brightness profiles. We show that neglect of the bulge contribution to the light profiles has a small and inconsequential effect on the distribution of μ_0 such that bimodality is never erased.

The outline of the paper is as follows: in §2, we briefly discuss our extraction of surface brightness profiles from isophotal fitting of the calibrated K' images originally obtained by T96. We describe in §3 the B/D decomposition code that we developed to analyse these profiles. This code relies on the modeling of various structural components that are defined in §4 and the fitting procedures are detailed in §5. Results are presented in §6 as we revisit the notion of structural bimodality based on our new data. An appendix includes the inferred structural parameters for the 65 UMa spiral galaxies.

2 SURFACE BRIGHTNESS PROFILES OF UMA CLUSTER GALAXIES

We have reanalyzed the K' photometry for the 65 Ursa Major galaxies reported in T96². Surface brightness profiles were extracted using the isophotal fitting method outlined in Courteau et al. (1996) and based on the astronomical data

² The calibrated images are publicly available at http://cadwww.hia.nrc.ca/astrocat/tully_help.html. Please see T96 for details about the observational set-up.

reduction package XVista³. The fitted isophotes along elliptical contours have a common center but the position angles and ellipticities are variable. These fits allowed for an independent determination of the K' -band surface brightness profile, contour ellipticity and total K' -band magnitude for each UMa galaxy. Our independent analysis of TV97's data will allow us to check if the reduction methods are a possible source of the observed bimodality.

A potential bias could arise through the contribution of the bulge component to the determination of μ_0 . TV97 computed the disk μ_0 by choosing by eye the radius at which the bulge would no longer contribute significantly to the overall profile, and fitting the outer SB profile, in magnitude units, as a straight line from that radius to the end of the profile. The disk μ_0 is the inward extrapolation of that fit to $r = 0$. This marking-the-disk technique works well on systems with little or no bulge but could potentially bias the disk μ_0 high in bulge-dominated systems. The observed bimodality could thus be due to systems with dominant bulges unaccounted for in the fits by eye⁴.

In §3 below, we introduce and make use of a B/D decomposition program to separate the bulge light from the disk profile and achieve, in principle, more realistic disk fits than TV97.

3 BULGE AND DISK DECOMPOSITIONS

The study of the photometric structure of a galaxy can benefit from the effective separation of the bulge light from the disk light. The motivation for bulge-to-disk (hereafter B/D) decompositions originated with de Vaucouleurs (1948), who distinguished between cuspy ($r^{1/4}$) and exponential surface brightness profiles of early to late-type galaxy bulges, respectively. However, many exceptions to the de Vaucouleurs profile as a description for galaxy bulges have since been found (Andredakis et al. 1995; Courteau et al. 1996; MacArthur et al. 2003; hereafter M03) and it is now generally accepted that the projected light profile of a 3D bulge is better fit by the generalized Sérsic function:

$$I(r) = I_0 \exp \left[- \left(\frac{r}{r_0} \right)^{1/n} \right] \quad (2)$$

where a Sérsic index of $n = 4, 1$, and 0.5 represents the de Vaucouleurs, exponential, and Gaussian profile, respectively.

Fitting the disk portion of the surface brightness profile has, traditionally, been a more straightforward task. De Vaucouleurs (1959) found that galaxy disks were best fit by a simple exponential function. The exponential distribution of all light and mass density distributions is indeed ubiquitous in most dynamically relaxed systems (Lin & Pringle 1987; Ferguson & Clarke 2001). However, significant deviations from this idealized distribution do exist. Outer truncations, characterized by a sudden plummeting of the light at large radii, have been observed in a large fraction of disk galaxies

³ <http://astronomy.nmsu.edu/holtz/xvista/index.html>

⁴ TV97 were aware of the potential bias in their fits and attempted to account for it. They speculated that the possible bias would not give rise to the observed bimodality.

(M03; Pohlen & Trujillo 2006). Typically, these breaks tend to occur in the face-on orientation between ~ 2 -3 disk scale lengths and are likely the result of disk instabilities (Debatista et al. 2006; Foyle et al. 2008). Similarly, the inner parts of galaxy disks exhibit departures from a pure exponential in galaxies with large bulges (M03). An inner disk truncation would explain the observed Freeman Type II galaxies, which show a deficit of light at the bulge-disk transition (Freeman 1970; M03). Finally, the presence of one or more spiral arms will cause a substantial excess of light over the underlying disk which will strongly affect any disk fit. Despite these observed deviations from an exponential profile, galaxy disks are still most often fit by a single pure exponential function.

We have implemented a code to model the different components of a galaxy based on its 1D azimuthally-averaged surface brightness profile. Our approach assumes that the galaxy bulge and disk are two photometrically and dynamically decoupled components and that the disk can be extrapolated towards the center of the galaxy⁵. The basic structure of our bulge-to-disk decomposition code follows from M03 and the majority of our assumptions and techniques are justified there. The code uses a non-linear least squares Levenberg-Marquardt technique (Press et al. 1993) to fit various combinations of functions to a given surface brightness profile. The bulge and disk light are modelled simultaneously and the best fit is selected to have the lowest global χ^2 value. For a thorough discussion of the reliability and accuracy of this technique, see M03 where the various errors have been carefully examined via Monte Carlo simulations. We have extended M03's technique to consider a broader variety of parameterizations for the bulge and disk light, as well as modelling other components such as nuclei and spiral arms as we describe below. We do not, however, model galaxy bars independently since these are not azimuthally symmetric and thus can have a variety of manifestations in a 1D profile. However, we will show later that our result is independent of the exclusion of this component.

Despite the significant insights gained from bulge-disk decompositions one must, however, recall the genuine limitations of our simplified parameterizations. For instance, the assumption of total decoupling between the bulge and disk may not be justified. However, there do not exist any data or simulations to falsify this hypothesis at present. Still, the B/D fitting parameters can be complemented by non-parametric measurements such as concentrations and effective radii, which allow a direct, unbiased comparison of galaxies across the full Hubble sequence (we explore the distribution of these other parameters, as applied to the Virgo cluster of galaxies, in McDonald et al. 2008).

4 LIGHT PROFILE MODELING

The light profile is a 1D representation of the radial distribution of light for a given galaxy. The shape of the light profile depends strongly on morphology, from the featureless exponential disk of LSB spiral galaxies, to the strongly bulged and spiral arm dominated HSB spiral galaxies, to

the nearly pure $r^{1/4}$ profiles of elliptical galaxies. In order to provide a parametric description of the light profile, various fitting functions are needed. Parameterizations for the nucleus, bulge, disk, spiral arms and disk truncation are discussed below.

4.1 Nucleus

It has become clear that most galaxies harbour either a bright compact nucleus in their center (Böker et al. 2002) or a supermassive black hole (SBH), or both (Côté et al. 2006). The typical half-light radius of a nucleus (< 15 pc; Côté et al. 2006) would cover ~ 1 -2 pixels on most ground-based detector with modest ($\sim 0.25''/\text{pix}$) resolution. These compact objects can be treated as a point source whose apparent width is determined by the ambient seeing. Compact nuclei differ significantly from the galaxy bulge both in brightness and extent. Nuclei are typically 100 times smaller than galaxy bulges and contribute, on average, 0.3%, and sometimes as much as 10%, of the total galaxy luminosity (Côté et al. 2006). For comparison, we find that the bulge of a typical Sb-Sc galaxy contributes roughly 10% of its total luminosity. We will treat galaxy nuclei as point sources, described by a delta function convolved with a Moffat function to simulate the effect of atmospheric turbulence (seeing).

Fig. 1 shows the effect of modelling a nucleus component on the surface brightness profile of a sample galaxy. This figure depicts a bulge-disk decomposition for a galaxy with an obvious nuclear component. If we allow an extra free parameter for the nucleus, a much better fit to all three components (nucleus, bulge, disk) is obtained. Without the fit to the nucleus, the bulge fit is forced to be cuspy, in order to account for this extra light at the center.

Note the dramatic effect of this extra component on the overall bulge-disk decomposition. A nucleus is only fitted if the residuals (lower panels in Fig. 1) in the very central parts of the galaxy are strongly negative.

4.2 Bulge

The bulge component of each galaxy is modelled as a generalized Sérsic (1968) function:

$$I_b(r) = I_e \exp \left\{ -b_n \left[\left(\frac{r}{r_e} \right)^{1/n} - 1 \right] \right\}, \quad (3)$$

or, in magnitudes,

$$\mu_b(r) = \mu_e + 1.0857 (b_n) \left[\left(\frac{r}{r_e} \right)^{1/n} - 1 \right] \quad (4)$$

where r_e is the radius which contains 50% of the total galaxy luminosity, or the effective radius. The total galaxy luminosity is determined by extrapolating the profile fit from $r = r_{max} \rightarrow \infty$ and adding this extrapolation to the total light within r_{max} . The effective surface brightness, I_e , is defined as the surface brightness at the effective radius. The parameter b_n ensures that r_e is the half-light radius. This parameter cannot be solved for analytically and we use the numerical approximations of Ciotti & Bertin (1999) and M03. The Sérsic index n allows for the fitting of dominant (e.g. de Vaucouleurs, $n = 4$) classical bulges, as are

⁵ See Baggett et al. 1998 for B/D modeling that accounts for a putative inner disk profile break.

observed in massive galaxies, as well as nearly exponential ($n = 1$) bulges in late-type spirals. By allowing the Sérsic index to vary from 0.1 to 10.0, we can fit a wide range of bulge shapes from LSB galaxies with $n \lesssim 0.5$ bulges to the most massive galaxies with $n \gtrsim 6$. The typical error in n is ~ 0.2 .

4.3 Disk

The radial density profile of a spiral galaxy disk is generally described by an exponential function of the form:

$$I_d(r) = I_0 \exp\left(-\frac{r}{h}\right), \quad (5)$$

or, in magnitudes,

$$\mu_d(r) = \mu_0 + 1.0857 \left(\frac{r}{h}\right), \quad (6)$$

where I_0 and μ_0 are the disk central surface brightness in intensity and magnitude units respectively, and h is the disk scale length. Eqs. 3 & 5 are equivalent for $n = 1$. The exponential function works well for galaxies with little or no radial structure like LSB disk galaxies. However, non-axisymmetric structures such as bars or spiral arms, and inner or outer profile truncations will induce departures from a pure exponential disk fit. Our modeling tries to account for these features. For disks with noticeable departures from the pure exponential model, the Sérsic function (Eq. (3)) is a better description.

High- n disk fits can describe the so-called Type III interacting galaxies (Erwin et al. 2005), while $n < 1$ fits can describe cored disks, found typically in dwarf systems. Fig. 2 shows how a Sérsic disk can yield a more compact bulge.

4.4 Spiral Arms and Rings

In azimuthally-averaged surface brightness profiles, both rings and spiral arms generally manifest themselves as smooth fluctuations above the underlying exponential disk (radial profile cuts would show more abrupt features). Assuming that rings and spiral arms represent an excess of light on top of the underlying disk, we mostly wish to trace the underlying exponential profile and clip any excess. We identify the starting point of any arm/ring by finding the locations where the surface brightness profile deviates positively from the mean exponential fit. The end point of the arm/ring will be the location where the surface brightness profile returns to the exponential fit value. If the isolated arm/ring region is found to have a smooth convex shape about the disk and lies beyond one disk scale length, then that region is excluded from the disk fit. The bulge and disk would be fit once more, with the clipped regions being excluded from the fit. This procedure is iterated until the extent of the arm/ring remains constant. Fig. 3 shows an example of this process. In addition to yielding a better disk fit, the exclusion of spiral arms in the B/D decomposition has a non-negligible effect on other galaxy components. It is clear from Fig. 3 that the nucleus and bulge fits are significantly altered by the removal of a spiral arm.

4.5 Outer Truncations

A topic of great interest in galaxy structure studies is that of disk truncations (Pohlen & Trujillo 2006; Roškar et al. 2008; Foyle et al. 2008). While the cause of these truncations remains unclear, their signatures as departures from the extrapolated inner disk to greater radii are easily identified, especially in edge-on galaxies. Because truncations may be mistaken for, or induced by, sky subtraction errors, care must be taken when measuring sky levels. An exact definition of disk truncation is still missing, however we choose to model them as the transition between an inner and outer exponential profiles governed by a Heaviside step function, $S(r)$, as in:

$$I_d(r) = I_{0,in} \exp\left\{\frac{-r}{h_{in}}\right\} \times (1-S) + I_{0,out} \exp\left\{\frac{-r}{h_{out}}\right\} \times S, \quad (7)$$

where

$$S = \frac{1}{[1 + \exp(r_t - r)]}. \quad (8)$$

For $r \ll r_t$, $S \rightarrow 0$ and the inner component dominates. For $r \gg r_t$, $S \rightarrow 1$ and the outer component dominates. This choice of fitting function requires that two additional parameters be defined; an outer disk scale length, h_{out} , and a truncation radius, r_t . The truncation radius is defined here as the radius where the disk fit is comprised of equal parts of each of the two exponential components. The parameter, $I_{0,out}$, is fixed such that the two disk components intercept at r_t . An example of B/D fitting with a profile break is shown in Fig. 4.

In our sample of 65 UMa galaxies, none have clearly defined truncations. However, although unused in this particular study, the ability to fit these peculiar cases is an important functionality of any bulge-disk decomposition code and will be more relevant in a future application to the richer and more exotic Virgo cluster (McDonald et al. 2008).

4.6 Seeing

Sharp light profile features, such as a galaxy nucleus or a cuspy bulge, are naturally blurred by the atmosphere. In order to model this effect, the bulge and nucleus fitting functions are convolved with a Moffat (1969) function whose FWHM matches the average seeing for each observation. The Moffat function is defined as:

$$I_{\text{PSF}}(r) = \frac{\beta - 1}{\pi \alpha^2} \left[1 + \left(\frac{r}{\alpha}\right)^2 \right]^{-\beta} \quad (9)$$

where β , the shape parameter, is taken to be 4.765 (Trujillo et al. 2001) and α is related to the FWHM via $\text{FWHM} = 2\alpha\sqrt{2^{1/\beta} - 1}$. The convolution of a point source with the seeing function yields satisfactory fits to the nucleus of our sample galaxies, as is seen in Fig. 1. The effect of numerical convolution on a Sérsic profile with $n = 4$ is shown in Fig. 5 and its inset. The effect of seeing for any profile with $n \gtrsim 2$ is indeed significant and seeing measurements, for the sake of bulge profile determination, should be determined carefully. Fortunately, the quantity that matters most for this study, the disk μ_0 , is only weakly affected by seeing. For computational efficiency, the convolution is only applied out to the radius where the fractional difference between the convolved and unconvolved profiles is $< 0.1\%$.

5 FITTING PROCEDURE

In order to converge upon a single decomposition for a given surface brightness profile, and having determined the types of galaxy components to fit, we now resort to a combination of grid search and generalized least-squares fitting to identify the best fitting functions. In the following sections the procedure from surface brightness profile to final decomposition is outlined in detail, inspired greatly by M03.

5.1 Initial Estimates

Non-linear least-squares fitting requires a set of initial guesses for the model parameters (Press et al. 1993). We can make use of various approximations guided by previous similar efforts (e.g. M03) to guess the best shape of a light profile with minimal computational effort; these are described below. For each parameter, several initial estimates are identified in order to achieve the best possible sampling of the χ^2 manifold.

5.1.1 Exponential Disk

The disk central surface brightness, μ_0 , and scale length, h , are first estimated with a marking-the-disk technique (Giovanelli et al. 1994; Courteau et al. 1996; TV97). This technique consists of fitting the surface brightness profile in magnitude scale with a straight line over a prescribed baseline. We adopt for our fits the radial range $r_e < r < r_{max}$, where r_e is the half-light radius of the total extrapolated light profile and r_{max} is the last reliable data point (with surface brightness error < 0.15 mag arcsec $^{-2}$), yielding the initial parameters μ_0 and h . This assumes that the outer profile at and beyond r_e is dominated by the disk component.

5.1.2 Sérsic Disk

The initial estimates for a Sérsic disk are the same as those used for the pure exponential disk. For a pure exponential disk, the following conversion applies:

$$\mu_e = \mu_0 + 1.822, \quad (10)$$

$$r_e = 1.678h. \quad (11)$$

These relationships arise from matching equations Eqs. 3 & 5 with $n = 1$ and $b_{n=1} = 1.678$.

5.1.3 Truncation Radius

The analysis of surface brightness profiles for face-on galaxies and profile cuts for edge-on galaxies have yielded a broad range in truncation radii, r_t , from 2.5 to 4.5 disk scale lengths (Pohlen & Trujillo 2006). Our general procedure uses, as first guess, $r_t \sim 0.5r_{max}$ and $r_t \sim 0.75r_{max}$. We find that our decompositions converge upon an acceptable truncation radius, as gauged by eye, when applicable. Recall that none of the UMa galaxies in this study show a significant disk truncation.

5.1.4 Sérsic Bulge

M03 identified 3 sets of initial parameters for galaxy bulges. The first set is determined empirically from observations of late-type field spirals (Courteau et al. 1996): $\mu_e = \mu_0$ and $r_e = 0.15h$, where μ_0 and h are measured from the marking-the-disk technique. We find exactly the same result for UMa galaxies in §6. The second set of initial parameters is obtained by first subtracting the marking-the-disk fit from the surface brightness profile. In an ideal case, the only remaining light would be that of the bulge and possibly a nucleus. The bulge effective surface brightness and radius are then measured directly from the residual profile, yielding the second set of initial bulge parameters. The third set of guesses comes from scaling r_e and μ_e to different values of the Sérsic n parameter (M03): $r_e = (b_n/0.4343)0.15h$ and $\mu_e = (b_n - b_{n=1}) + \mu_0$.

5.2 Grid Search

We have so far identified 5 types of profile fits: (i) single exponential, (ii) single Sérsic, (iii) Sérsic bulge plus exponential disk, (iv) Sérsic bulge plus Sérsic disk, and (v) Sérsic bulge plus a 2-component exponential disk. For each profile decomposition, our grid search involves 3 sets of initial parameters, as well as 3 different values for the seeing FWHM (the mean value and the high/low values corresponding to typical measurement errors of 15%). Finally, 100 different search values for the Sérsic n parameter were used for the bulge (0.1-10.0) and 20 for the disk (0.1-2.0), both in $\Delta n = 0.1$ increments. These values were held fixed during the fitting process in order to provide a more stable solution (M03). This set of parameters required 900 different fits for decompositions with a Sérsic bulge and one or two exponential disks and 6000 fits for decompositions with a Sérsic bulge and a Sérsic disk.

5.3 Fit Selection

In order to achieve a unique, best model solution, one must devise a scheme to discard unwanted fits. To narrow down our suite of hundreds or thousands of fits, we apply various rules in several stages which eventually yield a single fit. The first pass discards any fits that have not converged to a final solution after 50 iterations. This requirement ensures that any final solution is indeed a local minimum in the χ^2 space. Other constraints devised by M03 apply mostly to late-type spirals; our software only considers them in the case of a Sérsic bulge and exponential disk. These are:

1. $r_e > (0.3)^{1/n}(FWHM)$
2. $B/D < 5$
3. $r_e/h < 1$
4. $h < r_{max}$.

The first constraint requires that the size of the bulge be larger than the seeing disk; the second requires a reasonable B/D ratio (determined empirically for late-type galaxies); the third requires that the disk extends further than the bulge; and the fourth requires that the profile extends to at least one disk scale length.

Selection from the remaining fits is on the basis of both their global and inner χ^2 values, the latter being the χ^2 evaluated within half of a galaxy's effective radius (M03).

This process involves sorting the remaining fits in terms of their *inner* χ^2 , removing the lower half (worst solutions), then sorting the remaining fits by their *global* χ^2 and again removing the lower half. This process is iterated until less than 50 fits remained. At this point, the remaining fits are ranked based on both the global and inner χ^2 values and the fit that has the lowest total position on both lists is chosen. This process is applied to each of the 5 basic types of fits as described in §5.2. The best decomposition is the one with the lowest global χ^2 per degree of freedom. The global, rather than the inner, χ^2 is preferred here since the 5 different fits differ most strongly in their treatment of the outer profile.

6 UMA RESULTS

The results of the modeling of 65 UMa profiles with a Sérsic bulge and an exponential disk using the methodology described above, are presented in Table 1. The values of the disk μ_0 were corrected for inclination and extinction according to Eq. (1), assuming the transparent case ($C^K = 1$). The broad effect of performing a B/D decomposition should be to lower the measured disk μ_0 since we are now subtracting the bulge light from the profile. Interestingly, our B/D decomposition of the 65 K' -band UMa surface brightness profiles reveals results very similar to those obtained by TV97. Indeed, Fig. 6 shows the correlation between μ_0 and h as measured by TV97 and ourselves. Outliers with high bulge-to-total ratios are expected since TV97 did not parametrize the bulge and thus were unable to fully subtract the light it contributed to the disk. LSB outliers are likely due to disks with non-exponential profiles which the eye will fit very differently than an automated process.

Before determining the distribution of disk central surface brightnesses, we can verify the adequacy of the exponential function to characterize galaxy disks. Fig. 7 shows the distribution of the Sérsic n parameter for the extended component of galaxies in our sample. The peak of this distribution around $n = 1.0$ suggests that the exponential function is generally a suitable fitting function for galaxy disks. However, there exists galaxies with high- n values (S0s) and with low- n values (typically irregular or dwarfs) suggesting that parameterizing all disks with the same function may be hazardous. The two high- n outliers in Fig. 7 correspond to profiles which have a smooth transition between bulge and disk and thus were best fit by a single Sérsic function, yielding a cuspy profile. We return to this topic at the end of the section by using a Sérsic function rather than the exponential to derive the distribution of disk surface brightnesses.

The distribution of inclination-corrected disk $\mu_{0,K}^i$, shown in Fig. 8 for 65 UMa galaxies is clearly bimodal with peaks, as fit by two Gaussians, at 20.0 and 17.8 K' mag arcsec $^{-2}$. These values can be compared with TV97's reported peaks at 19.7 and 17.3 K' mag arcsec $^{-2}$. Within the errors, the location of our and TV97's peaks are the same. This excellent agreement between the marking-the-disk technique and B/D decompositions has been shown in previous studies (e.g. de Jong 1996). However, this represents the first test of this kind using TV97's basic data, confirming the adequacy of their analysis.

In order to gauge the strength of the bimodality, we use

the statistical F test which compares two different fitting functions for a single set of data. We find that the distribution of disk central surface brightnesses for the 65 galaxies in this sample is better fit with a pair of Gaussians, rather than a single Gaussian, with 80% confidence. If we remove galaxies that do not exhibit a clear exponential disk (e.g. S0s) from this sample, the confidence level increases to 85%.

Fig. 9 shows the relationship between μ_0 and disk scale length, h . In this figure, the diagonal lines of constant luminosity intersect both HSB (filled squares) and LSB (open squares) points. At intermediate luminosity, there can be both HSB and LSB galaxies (a high central surface brightness and small h , or a low central surface brightness and large h). The fact that two galaxies with the same luminosity can have wildly different surface brightnesses leads to the belief that some mechanism, perhaps related to the initial halo spin parameter, prevents LSB systems from collapsing to the same densities as HSBs (e.g. Dalcanton et al. 1997).

Fig. 9 makes obvious that for a given luminosity, the LSB galaxy must be more extended than the HSB galaxy. With this small sample, no LSB galaxy exceeds $10^{11} L_{\odot}$. Applying the statistical F test to the distribution of disk scale lengths yields a bimodality confidence level of 60%, implying that this distribution is not likely bimodal, as is clear by eye.

We look in Fig. 10 for a possible correlation between the observed bimodality in $\mu_{0,K}^i$ and the near-IR luminosity function. The distribution of total luminosities is strongly bimodal at K' band, even though the correlation between the disk central surface brightness and the total luminosity of a galaxy is weak. There appears to be a strong preference towards either $K'_{TOT}=8$ mag or $K'_{TOT}=11$ mag, with a large (~ 2 mag) gap with few galaxies. This bimodality in total magnitude is immediately apparent by eye, with an F-test yielding a confidence level of 85%⁶. There also appears to be an almost equal mix of high and low surface brightness disks for bright galaxies, while faint galaxies are dominated by LSB disks. However, it should be noted that several of the bright galaxies (primarily S0s) do not have pure exponential disks, and the measurement of μ_0 in this case will yield a low and likely meaningless estimate.

It is natural to ask if the bimodality in the disk μ_0 is correlated with any bulge structure. Fig. 11 shows the disk central surface brightness as a function of the bulge-to-total ratio, B/T . We can clearly assert that the surface brightness bimodality of disk galaxies and the well known observed color (or morphological) bimodality (e.g. Strateva et al. 2001) are independent. Galaxies with large bulges (typically redder, e.g. S0-Sb) or galaxies with little-to-no bulge (typically bluer, e.g. Sc-Irr) all exist in the form of HSB or LSB disks.

Another way to illustrate the connection between bulges and disks is shown in Fig. 12. Here we see a strong correlation between the bulge effective surface brightness and the disk effective surface brightness (Pearson $r=0.67$), using

⁶ TV97 only discussed the luminosity function at B band which is flat rather than bimodal. High luminosity galaxies tend to be redder than low luminosity galaxies which increases the separation between these types, resulting in the observed minimum in the luminosity function at K' band.

Eq. 10 to convert from μ_0 to μ_e . The striking bimodality that is apparent in disk surface brightness is not seen in the bulge. From this strong correlation, it is clear that bright disks tend to harbor bright bulges, while faint disks tend to harbor faint bulges (or none at all).

As mentioned in §2 we do not independently fit for galaxy bars in our B/D decompositions. For weak bars, the bulge absorbs most of their signal. We must however verify that stronger bars do not skew B/D parameters to the point of inducing a brightness bimodality. Fig. 13 shows the distribution of μ_0 for galaxies with and without a bar (the morphological type is taken from the Nasa Extragalactic Database [NED]). Bimodality is clearly seen in both sub-samples, albeit with weaker F-statistics than for the full sample since the number of objects in each sub-samples is less. Fig. 13 shows that bimodality is not the result of bar structure.

Finally, it is unnecessary to restrict ourselves to the choice of an exponential function to describe the disk of a galaxy. We report in Fig. 14 the results of fitting two Sérsic functions to model the bulge and disk of the galaxy. This more generalized approach preserves the bimodality of the disk surface brightness, giving a bimodality confidence level of 60%. The peaks in this case are shifted by roughly 1.8 mag from those seen in Fig. 8, which corresponds to the difference in measurement between central and effective surface brightness (Eq. 10). This fitting method also provides us with a way of testing the ubiquity of the exponential disk. We find that the “disks” in this sample have $\langle n \rangle = 0.8$ with $\sigma = 0.3$. So, while the vast majority of our disks are nearly exponential (see Fig. 7), there is a broad distribution in shapes that are best described with B/D profile decompositions.

7 A DYNAMICAL EXPLANATION?

The two surface brightness peaks identify two distinct regimes of stellar surface density. Could this structural bimodality be linked to any dynamical process? It is known that HSB and LSB galaxies have different rotation curve characteristics. HSB galaxies typically achieve maximal rotation speed at or within $r = 2.15h$ (e.g. Courteau 1997) while the rotation curves of LSB galaxies are still rising at that radius. For HSB galaxies the baryonic disk component may substantially dominate the halo interior to $2h$ while for LSBs, the baryons are sub-dominant to the dark matter component at nearly all galactocentric radii. This conclusion is supported by mass modeling and dynamical arguments (e.g. Courteau & Rix 1999; Dutton et al. 2005; Dutton et al. 2007). The proposed explanation offered by TV97 for this phenomenon was that of two stable radial configurations for the baryons in galaxies, an idea proposed by Mestel (1963). The configuration occupied by the LSB galaxies would arise from small-amplitude ($\sim 1\sigma$) initial fluctuations and thus that have formed late with high angular momentum. Material from the disk in these systems is not sufficiently funneled to the center due to their high angular momentum to ever dominate the dark halo (Dalcanton et al. 1997). The alternate configuration involves galaxies either with low initial angular momentum or with baryon content that loses angular momentum through interactions.

Material with minimal angular momentum can collapse far enough to dominate the dark halo in the inner regions. There would be a threshold amount of angular momentum that determines whether the disk collapses to a HSB configuration or is unable to fully collapse and “stalls” as an LSB galaxy.

In order to assess any dynamical connection with surface brightnesses, we obtained HI line widths from Marc Verheijen (Verheijen & Sancisi 2001) for 62 UMa galaxies. The distribution of rotational velocities, corrected for inclination, for those galaxies is shown in Fig. 15. Not only is there a clear bimodality in the μ_0 distribution, but there is also one in the distribution of rotational velocities. Yet the correlation between rotational velocity and surface brightness is relatively weak ($r = 0.7$). By virtue of the Tully-Fisher relation (Tully & Fisher 1977), this is expected from Fig. 10. There is a minor concern that LSB galaxies may reach a maximum rotation velocity at larger physical radii than HSB galaxies of the same luminosity (TV97). A contribution toward bimodality in V_{max} could thus arise from not sampling the rotation curve far enough for LSB galaxies. If our V_{max} term is calculated at a limiting isophotal radius (say, r_{max}), then it is plausible that the HSB galaxies will have $V(r_{max}) = V_{max}$ whereas the LSB galaxies only have $V(r_{max}) = aV_{max}$ where potentially $a < 1$ in some cases.

We explore in greater detail in our companion paper on the light profiles and luminosity function of Virgo cluster galaxies (McDonald et al. 2008) the suite of possible scenarios that may explain the observed structural bimodality in cluster galaxies, including cluster-induced morphological transitions, gas depletion and/or dynamical thresholds in a cluster environment.

Unlike traditional rich clusters such as Virgo, with a space density of $\sim 100 \text{ Mpc}^{-3}$, UMa closely resembles the field with a space density of only 8 Mpc^{-3} (TV97; Trentham & Tully 2002). Furthermore, we have confirmed TV97’s finding that the surface brightness bimodality is enhanced when only the most isolated galaxies in UMa are considered. This suggests that the intermediate surface brightness gap may be filled by galaxies found preferentially in dense environments: dwarf and giant ellipticals. A follow-up study in a rich cluster will allow a complete morphological sampling, ensuring that bimodality is not due to the absence of some classes of galaxy.

Follow-up near-IR surveys of both field and cluster populations will be needed to determine the environmental dependence on the structural bimodality. Previous studies of the surface brightness distribution in the field have relied on optical data which requires a complicated, and not fully understood, deprojection of the surface brightness profiles to the face-on case. The near-IR field galaxy surveys collected to date have traditionally been too shallow to properly sample the LSB peak (e.g. de Jong 1996; Jarrett et al. 2003; Grauer et al. 2003; M03). A deep, near-IR survey of a larger cluster such as Virgo, Fornax or Coma is needed to assess the cluster dependence of our result and whether UMa’s surface brightness distribution is typical. Since galaxy clusters are confined structures, they are an ideal laboratory for a study of this type since volume corrections are less significant. Note that none of the nearby clusters listed above

will be covered in any deep fashion by the ongoing UKIDSS survey⁷.

Finally, though more expensive observationally than a simple photometric investigation, a complete dynamical study of a cluster environment will ultimately be needed to pin down the cause of structural bimodality. Galaxy line widths are currently available mostly for HSB galaxies and their sources are often heterogeneous. A dedicated dynamical survey down to low rotational velocities could not only assess the bimodality of the velocity function of cluster galaxies, in conjunction with that of the luminosity function, but also examine whether those functions are related in any way to the shape of the rotation curve and/or the distribution of visible to dark matter in galaxies.

8 CONCLUSION

We have implemented a new code for bulge-disk decompositions which accounts for compact nuclei, seeing, spiral arms and disk truncations. We also allow for both exponential and Sérsic bulges and disks. By carefully fitting all the components of a given galaxy, we can extract confident estimates of the various galaxy structural parameters.

We have confirmed the bimodality of disk central surface brightness as reported by TV97 and, in addition, find a distinct minimum in the near-IR luminosity function at $K' \simeq 9$ ($M_K \sim -22$) and a corresponding minimum in the distribution of maximal rotational velocities for UMa galaxies. The concern about small number statistics is, however, real (Bell & de Blok 2000). Furthermore, the UMa cluster population resembles that of the field and a sample that includes more early type galaxies would offset any ambiguities arising from morphological dependencies. A new near-IR based study of a richer, denser, more evolved cluster is needed (see McDonald et al. 2008). Likewise, a statistically complete sample of field galaxies would address possible environmental dependence of the observed galaxy structural bimodality.

9 ACKNOWLEDGEMENTS

We acknowledge Lauren MacArthur for useful conversations and suggestions about bulge-disk decompositions and Marc Verheijen for providing the raw Ursa Major photometry and line widths. We thank the referee, Enrico Maria Corsini, for his careful read of the paper and the suggestion to confirm that bimodality is not linked to galaxy bars. SC would like to acknowledge financial support via a Discovery Grant from the National Science and Engineering Council of Canada. RBT acknowledges support from US National Science Foundation award AST 03-07706.

This research has made use of (i) the NASA/IPAC Extragalactic Database (NED) which is operated by the Jet Propulsion Laboratory, California Institute of Technology, under contract with the National Aeronautics and Space Administration, as well as NASA's Astrophysics Data System; (ii) the *Sloan Digital Sky Survey* (SDSS). Funding for the creation and distribution of the SDSS

Archive has been provided by the Alfred P. Sloan Foundation, the Participating Institutions, the National Aeronautics and Space Administration, the National Science Foundation, the U.S. Department of Energy, the Japanese Monbukagakusho, and the Max Planck Society. The SDSS Web site is <http://www.sdss.org/>. The SDSS is managed by the Astrophysical Research Consortium (ARC) for the Participating Institutions. (iii) the HyperLeda database (<http://leda.univ-lyon1.fr>).

REFERENCES

- Andredakis, Y. C., Peletier, R. F., & Balcells, M. 1995, MNRAS, 275, 874
- Bell, E. F., & de Blok, W. J. G. 2000, MNRAS, 311, 668
- Böker, T., Laine, S., van der Marel, R. P., Sarzi, M., Rix, H.-W., Ho, L. C., & Shields, J. C. 2002, AJ, 123, 1389
- Ciotti, L., & Bertin, G. 1999, A&A, 352, 447
- Côté, P., et al. 2006, ApJS, 165, 57
- Courteau, S., de Jong, R. S., & Broeils, A. H. 1996, ApJ, 457, L73
- Courteau, S. 1997, AJ, 114, 2402
- Courteau, S., & Rix, H.-W. 1999, ApJ, 513, 561
- Courteau, S., Dutton, A. A., van den Bosch, F. C., MacArthur, L. A., Dekel, A., McIntosh, D. H., & Dale, D. A. 2007, ApJ, 671, 203
- Dalcanton, J. J., Spergel, D. N., & Summers, F. J. 1997, ApJ, 482, 659
- Debattista, V. P., Mayer, L., Carollo, C. M., Moore, B., Wadsley, J., & Quinn, T. 2006, ApJ, 645, 209
- de Jong, R. S. 1996, A&A, 313, 45
- de Vaucouleurs, G. 1948, Annales d'Astrophysique, 11, 247
- de Vaucouleurs, G. 1959, Handbuch der Physik, 53, 311
- Dutton, A. A., Courteau, S., de Jong, R., & Carignan, C. 2005, ApJ, 619, 218
- Dutton, A. A., van den Bosch, F. C., Dekel, A., & Courteau, S. 2007, ApJ, 654, 27
- Erwin, P., Beckman, J. E., & Pohlen, M. 2005, ApJ, 626, L81
- Ferguson, A. M. N., & Clarke, C. J. 2001, MNRAS, 325, 781
- Foyle, K., Courteau, S., & Thacker, R. J. 2008, MNRAS, 386, 1821
- Freeman, K. C. 1970, ApJ, 160, 811
- Giovanelli, R., Haynes, M. P., Salzer, J. J., Wegner, G., da Costa, L. N., & Freudling, W. 1994, AJ, 107, 2036
- Grauer, A. D., Rieke, M. J., & Quillen, A. C. 2003, ApJS, 149, 327
- Jarrett, T. H., Chester, T., Cutri, R., Schneider, S. E., & Huchra, J. P. 2003, AJ, 125, 525
- Lin, D. N. C., & Pringle, J. E. 1987, ApJ, 320, L87
- MacArthur, L. A., Courteau, S., & Holtzman, J. A. 2003, ApJ, 582, 689
- Mestel, L. 1963, MNRAS, 126, 553
- Moffat, A. F. J. 1969, A&A, 3, 455
- Paturel, G., Petit, C., Prugniel, P., Theureau, G., Rousseau, J., Brouty, M., Dubois, P., & Cambrésy, L. 2003, A&A, 412, 45
- Paturel, G., Theureau, G., Bottinelli, L., Gouguenheim, L., Coudreau-Durand, N., Hallet, N., & Petit, C. 2003, A&A, 412, 57
- Pohlen, M., & Trujillo, I. 2006, A&A, 454, 759
- Press, W. H., et al. 1993, The Observatory, 113, 214
- Roškar, R., Debattista, V. P., Stinson, G. S., Quinn, T. R., Kaufmann, T., & Wadsley, J. 2008, ApJ, 675, L65
- Sérsic, J. L. 1968, Cordoba, Argentina: Observatorio Astronómico, 1968,
- Strateva, I., et al. 2001, AJ, 122, 1861
- Trentham, N., & Tully, R. B. 2002, MNRAS, 335, 712

⁷ <http://www.ukidss.org/>

- Trujillo, I., Aguerri, J. A. L., Cepa, J., & Gutiérrez, C. M. 2001, MNRAS, 321, 269
- Tully, R. B., & Fisher, J. R. 1977, A&A, 54, 661
- Tully, R. B., Verheijen, M. A. W., Pierce, M. J., Huang, J.-S., & Wainscoat, R. J. 1996, AJ, 112, 2471
- Tully, R. B., & Verheijen, M. A. W. 1997, ApJ, 484, 145
- Verheijen, M. A. W., & Sancisi, R. 2001, A&A, 370, 765

Table 1: B/D Parameters

(1)	(2)	(3)	(4)	(5)	(6)	(7)	(8)	(9)	(10)	(11)	(12)	(13)	(14)
PGC	T	K'_T	b/a	B/T	C_{28}	μ'_e	r'_e	$\mu'_{e,d}$	$r'_{e,d}$	$\mu'_{e,b}$	$r'_{e,b}$	n'_b	μ'_{nuc}
34971	Sm	11.22	0.31	0.00	2.97	21.47	31.81	20.47	38.32				17.98
35202	Sd	11.36	0.98	0.05	2.30	20.94	19.20	21.53	30.99	20.77	8.56	0.30	17.42
35676	SBc	7.83	0.58	0.03	1.93	19.81	73.65	19.37	76.97	17.44	5.87	0.60	14.77
35711	SBa	8.64	0.56	0.03	2.78	18.79	32.22	18.48	35.51	17.52	3.75	0.40	14.31
35999	SBb	9.13	0.33	0.00	2.91	18.83	24.62	17.94	29.06				15.44
36136	SBcd	10.77	0.37	0.00	2.44	20.01	20.56	19.05	23.32				21.92
36343	Scd	11.17	0.11	0.03	3.12	21.88	40.70	20.34	65.16	19.80	10.91	0.40	17.68
36528	Sm	11.74	0.74	0.03	2.42	21.15	22.71	21.64	32.92	21.80	9.42	0.50	18.60
36686	S0	10.79	0.58	0.38	3.52	18.36	8.21	19.00	13.18	16.97	5.19	0.50	14.05
36699	Sc	7.75	0.20	0.07	4.16	18.79	47.25	18.09	64.43	16.28	3.88	0.70	14.61
36825	Im	11.73	0.53	0.00	2.60	20.89	21.07	20.72	25.63				18.08
36875	SBc	7.51	0.75	0.48	4.09	19.09	46.54	20.35	82.48	17.80	23.34	1.20	13.68
36897	SB0/a	11.31	0.63	0.14	3.50	20.00	13.49	20.34	21.61	18.51	4.58	0.40	17.17
36953	SBd	10.43	0.93	0.13	1.96	20.37	24.25	20.09	25.43	19.06	12.50	0.20	16.84
36990	S0	11.64	0.78	0.07	3.08	17.58	4.20	17.69	5.12	17.92	2.05	0.10	16.76
37024	Sd	10.59	0.85	0.16	3.74	19.73	17.25	20.25	23.97	18.62	4.76	1.00	17.28
37036	Scd	9.03	0.24	0.01	2.68	20.26	54.91	19.33	64.37	18.64	4.02	0.20	17.20
37037	IBm	11.64	0.93	0.00	1.73	22.00	23.23	21.61	26.20				19.29
37038	SB?	11.86	0.46	0.00	2.76	20.99	19.48	20.44	22.91				22.96
37073	S0	10.65	0.82	0.19	4.58	18.64	9.48	18.96	13.29	17.51	2.46	0.60	12.23
37136	Sb	9.72	0.97	0.31	4.65	17.54	7.52	18.42	13.30	15.63	2.49	0.70	12.46
37164	SBm	12.85	0.29	0.00	2.31	21.59	17.19	20.60	21.03				19.66
37217	Sm	12.08	0.81	0.00	2.31	21.27	21.44	21.54	27.16				17.39
37229	Sc	7.74	0.88	0.07	3.24	18.96	46.66	19.07	55.55	17.30	6.48	0.80	15.44
37290	Sbc	8.45	0.63	0.05	3.31	18.42	27.55	18.05	29.81	16.95	4.77	0.30	15.27
37306	SBbc	6.99	0.45	0.13	3.70	18.79	60.11	18.61	83.48	16.87	11.31	1.50	14.09
37418	Scd	12.58	0.16	0.00	2.45	21.84	21.85	20.20	26.09				26.40
37466	Sbc	9.39	0.24	0.03	3.13	20.00	39.22	19.22	54.36	18.12	4.35	0.70	16.22
37520	SBb	8.81	0.86	0.05	2.36	17.64	17.03	17.76	18.28	16.92	2.61	0.20	11.83
37525	SBm	10.50	0.52	0.05	2.55	21.14	38.80	21.11	52.49	19.38	10.18	0.20	17.92
37542	SBm	10.07	0.72	0.08	3.31	19.44	19.12	19.10	21.00	17.87	4.33	0.20	16.79
37550	Scd	12.00	0.75	0.11	3.11	20.02	10.61	20.26	14.20	19.60	4.66	0.30	17.93
37553	Im	11.14	0.47	0.14	3.74	19.82	14.59	20.36	26.41	19.08	5.62	0.60	17.85
37584	SBd	10.18	1.00	0.06	2.40	20.62	30.17	20.75	38.88	19.57	8.97	0.30	17.95
37617	SBbc	7.14	0.54	0.09	3.68	19.70	78.95	18.97	92.48	16.61	8.42	1.10	13.07
37621	Scd	14.08	0.24	0.00	3.62	21.93	10.82	21.22	16.25				19.98
37642	S0	7.35	0.82	0.38	5.33	16.87	15.68	18.09	34.77	14.87	6.12	0.80	11.38
37682	SBm	12.52	0.57	0.00	2.16	22.15	22.53	22.10	31.93	21.32	1.67	0.20	18.74
37691	Sb	7.77	0.16	0.01	3.20	18.70	45.93	17.38	53.81				12.66
37692	SBcd	9.83	0.72	0.01	2.48	19.98	31.15	20.00	39.11	20.06	5.22	0.40	17.10
37697	SBd	9.51	0.12	0.05	2.91	20.16	38.27	18.82	63.82	18.48	16.78	0.20	16.88
37700	Im	12.92	0.38	0.00	2.14	21.49	16.36	21.27	24.04	22.87	1.87	0.10	18.31
37719	Sab	8.20	0.40	0.01	4.15	16.81	15.07	16.05	16.93				13.70
37735	SBcd	11.36	0.45	0.08	2.68	21.28	25.92	20.74	32.01	19.82	9.53	0.40	17.90
37760	S0	7.67	0.22	0.55	5.91	16.86	16.25	18.40	53.66	16.40	13.31	1.80	13.28
38068	SBbc	8.00	0.51	0.17	4.73	19.92	63.56	19.23	63.66	16.35	4.99	1.70	12.93
38283	SBc	9.18	0.23	0.05	3.87	18.66	21.76	17.96	29.61	18.43	4.96	0.90	16.02
38302	SBbc	7.56	0.43	0.01	2.82	19.30	63.63	18.00	49.63				12.93
38356	Sdm	11.22	0.25	0.00	2.33	21.36	33.01	20.45	45.96				18.43
38370	SBb	8.06	0.31	0.07	2.94	19.46	57.87	18.49	55.11	16.34	4.47	0.40	14.36
38375	Sdm	11.91	0.38	0.00	2.62	20.93	19.31	20.23	21.96				25.25
38392	SBb	7.90	0.57	0.50	6.24	16.95	12.83	18.76	37.34	15.30	6.52	0.80	11.25
38440	S0	7.60	0.22	0.66	5.69	16.08	11.13	18.35	47.74	15.75	12.46	1.70	12.37
38503	S0	10.05	0.43	0.48	4.32	18.14	10.62	19.22	21.26	17.17	7.90	0.80	12.35
38507	S0	12.45	0.60	0.20	3.52	20.78	10.59	21.25	19.89	19.09	4.78	0.60	17.83
38643	S0	8.14	0.62	0.14	4.16	17.75	22.00	17.60	26.39	15.37	3.19	0.70	11.37

Table 1: B/D Parameters

(1)	(2)	(3)	(4)	(5)	(6)	(7)	(8)	(9)	(10)	(11)	(12)	(13)	(14)
PGC	T	K'_T	b/a	B/T	C_{28}	$\mu_e^{K'}$	$r_e^{K'}$	$\mu_{e,d}^{K'}$	$r_{e,d}^{K'}$	$\mu_{e,b}^{K'}$	$r_{e,b}^{K'}$	$n_b^{K'}$	$\mu_{nuc}^{K'}$
38654	SB0	7.82	0.54	0.30	5.18	16.82	13.99	17.44	26.92	15.06	4.47	1.10	13.52
38795	SBb	7.51	0.17	0.00	3.54	18.96	55.18	16.96	52.03				13.84
38951	Im	12.18	0.61	0.01	1.30	21.85	25.94	21.59	31.27	21.09	3.85	0.10	17.52
38988	Scd	9.84	0.14	0.06	3.52	20.55	38.91	19.70	67.94	18.68	8.85	0.70	16.71
39237	Sa	10.71	0.58	0.01	2.40	19.21	14.27	19.48	18.39				15.63
39241	Sb	7.67	0.17	0.06	3.23	19.62	67.27	17.90	71.35	17.72	14.89	0.90	14.56
39285	S0	8.37	0.29	0.10	4.16	18.06	24.81	17.63	33.14	16.67	4.39	1.00	14.81
39344	Sdm	12.90	0.15	0.08	3.20	22.43	24.08	21.52	37.93	20.50	7.21	0.30	18.43
40228	SB0	8.22	0.32	0.33	5.75	17.17	13.56	17.96	35.92	15.37	4.90	0.80	12.78

Table captions – Col.(1) PGC number; Col.(2) Morphology from the NASA Extragalactic Database; Col.(3) Total K' magnitude; Col.(4) Ratio of the minor-to-major axis diameters; Col.(5) Ratio of the bulge to the total luminosity; Col.(6) Galaxy concentration, defined as $C_{28} = 5 \log(r_{80}/r_{20})$ where r_{20} and r_{80} are radii enclosing 20% and 80% of the total light, respectively; Col.(7) Effective surface brightness, defined as the surface brightness at the galaxy half-light radius; Col.(8) Effective radius within which half of the total galaxy light is enclosed; Col.(9) Effective surface brightness of the disk; Col.(10) Half-light radius of the disk; Col.(11) Effective surface brightness of the bulge; Col.(12) Half-light radius of the bulge; Col.(13) Sérsic parameter for the bulge; Col.(14) Surface brightness of the galaxy nucleus.

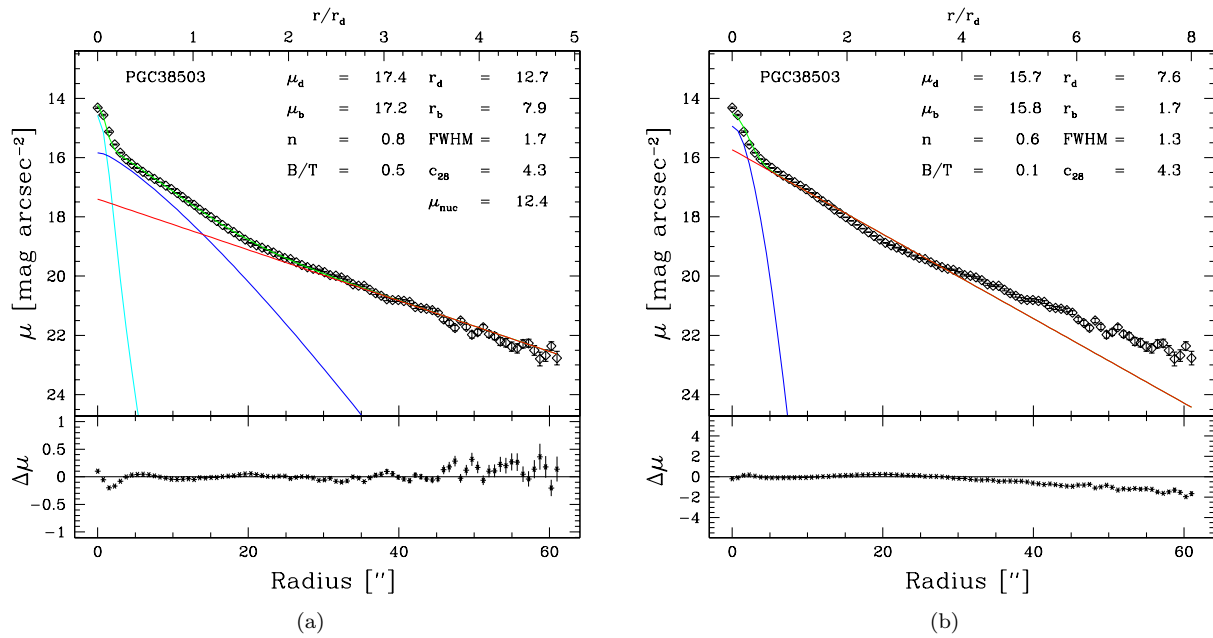


Figure 1. B/D decompositions of K' -band surface brightness profile with a central nucleus (a) and without (b). The justification for a nucleus component seems obvious in this case. The red line is the disk (exponential) fit, the blue line is the bulge (Sérsic) fit and the cyan line is the fit to the nucleus. The decomposition parameters all refer to the K' -band.

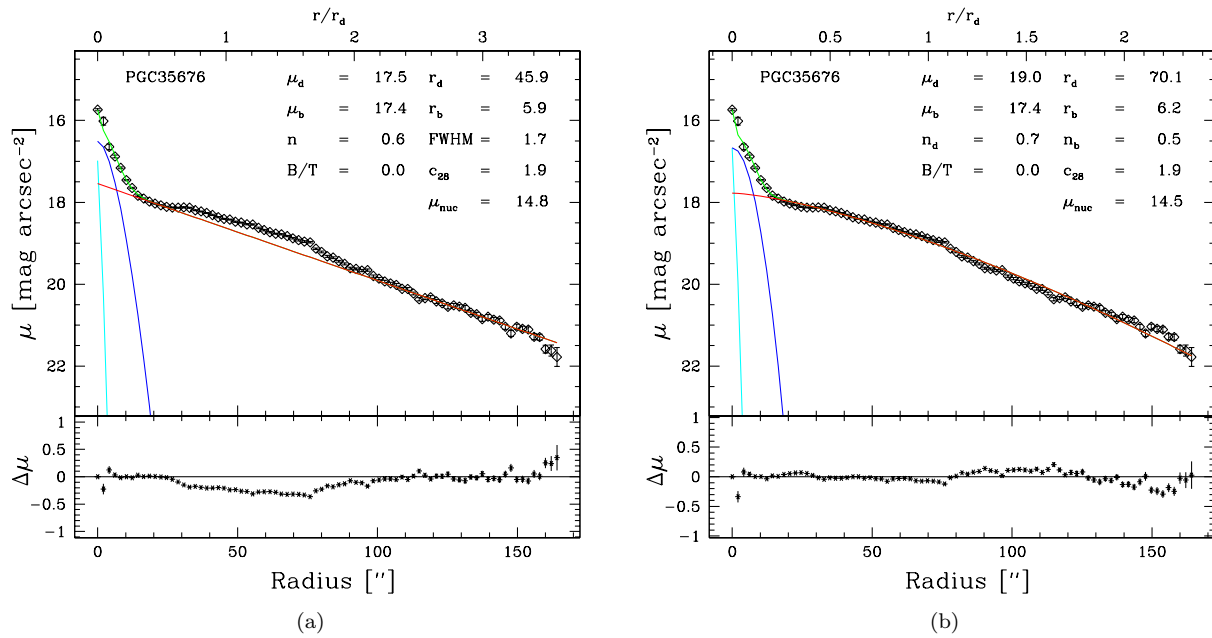


Figure 2. Bulge-disk decompositions with an exponential (a) and Sérsic (b) disk. The decomposition all parameters refer to the K' -band.

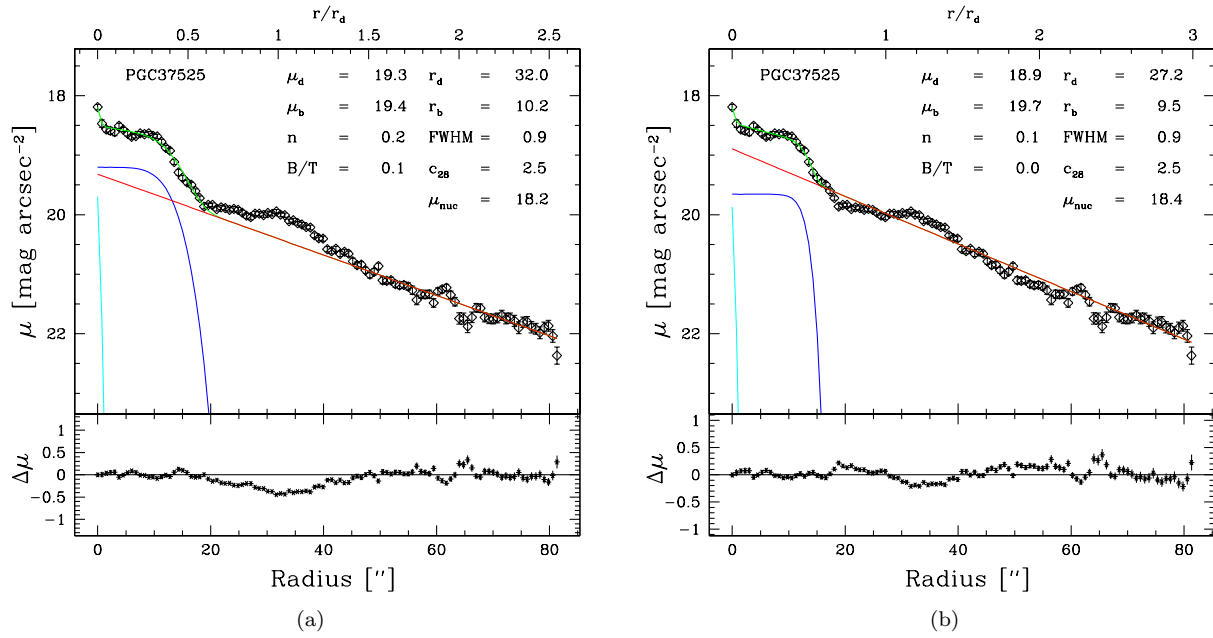


Figure 3. Bulge-disk decompositions with (a) and without (b) spiral arm clipping. The decomposition parameters all refer to the K' -band.

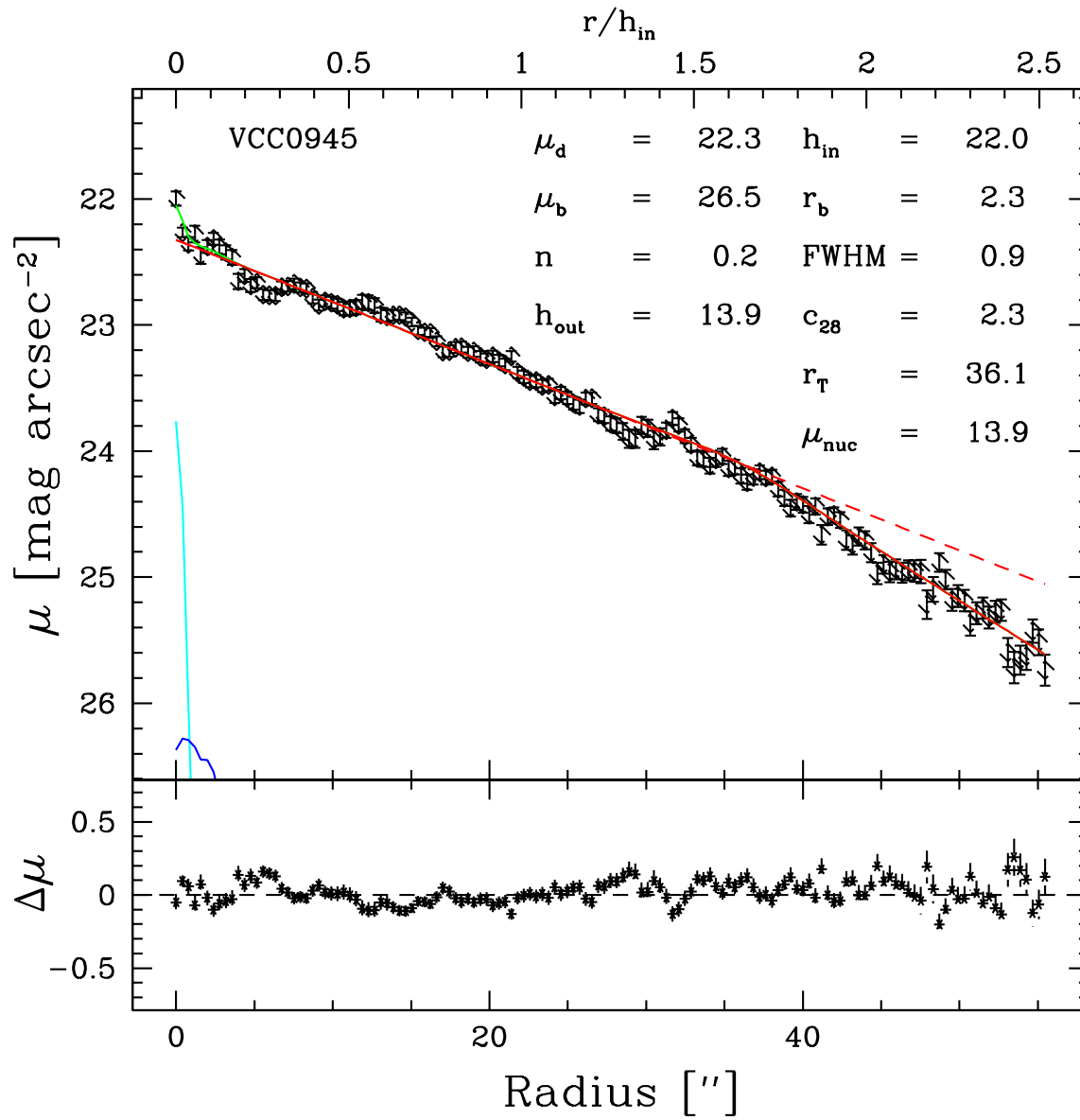


Figure 4. Example of a B/D decomposition for a Virgo cluster galaxy with an outer truncation. The two-component disk fit with two exponentials is governed by a simple step function. The decomposition parameters all refer to the r -band.

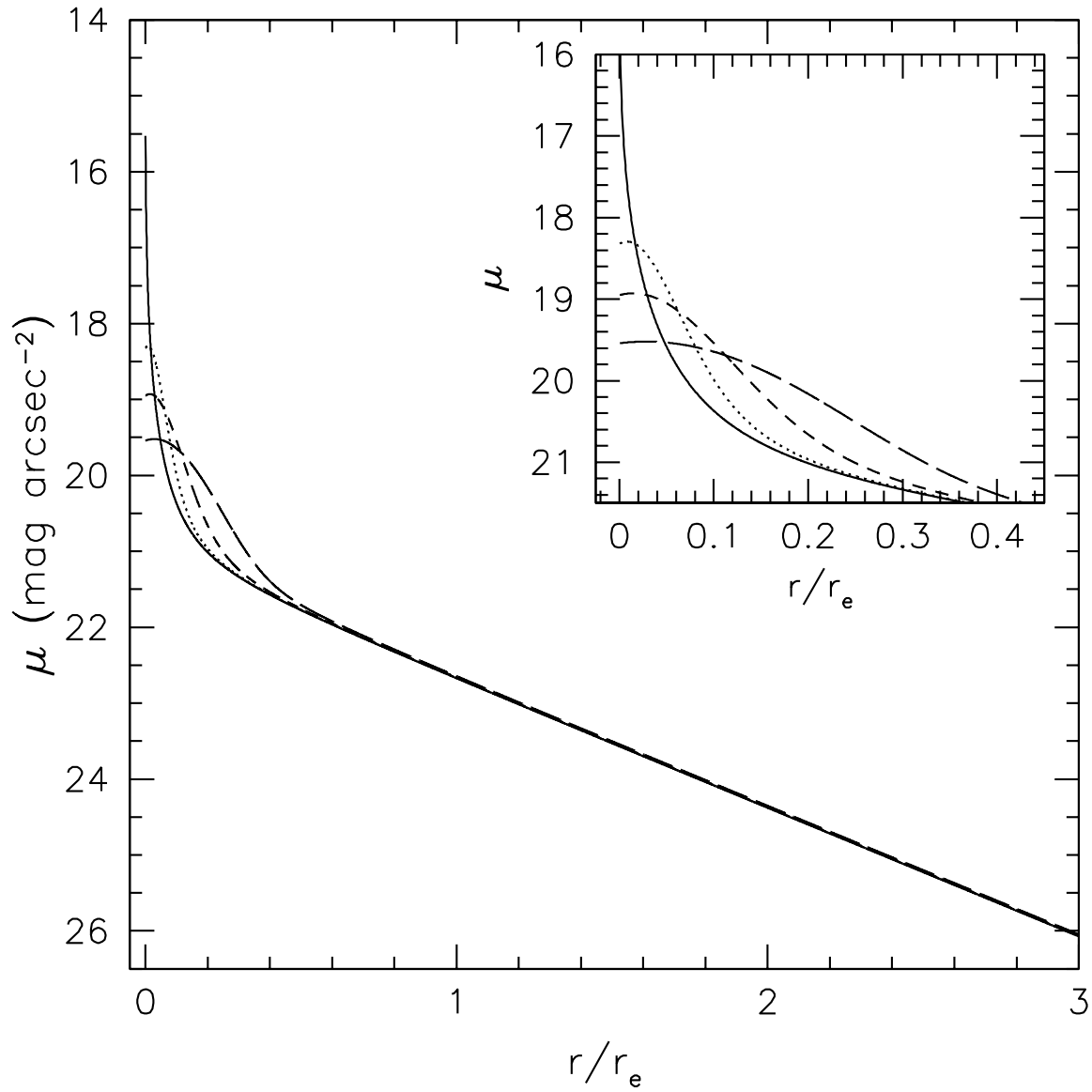


Figure 5. Example of a model $n = 4$ Sérsic bulge and exponential disk (solid) convolved with a Moffat function of FWHM=2'' (dotted), FWHM=4'' (short dash) and FWHM=8'' (long dash). The inset shows a magnified portion of the inner profile.

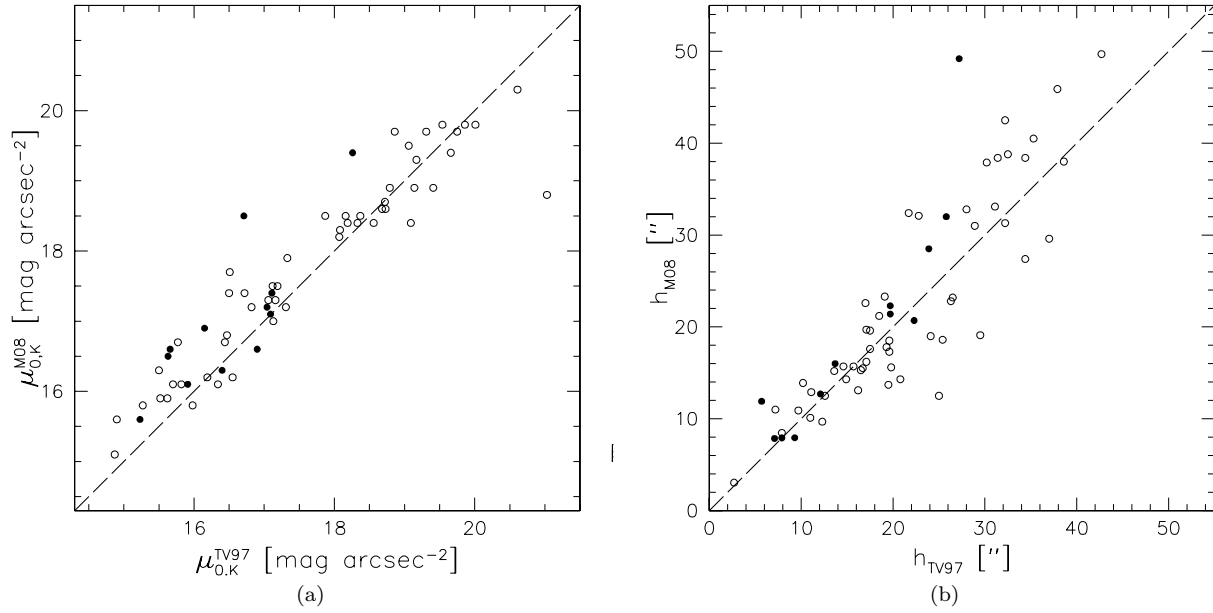


Figure 6. Comparison of measured (a) μ_0 and (b) h as published by TV97 and from our bulge-disk decompositions. The open circles are galaxies with bulge-to-total (B/T) ratios of less than 20%, while the filled circles have B/T greater than 20%.

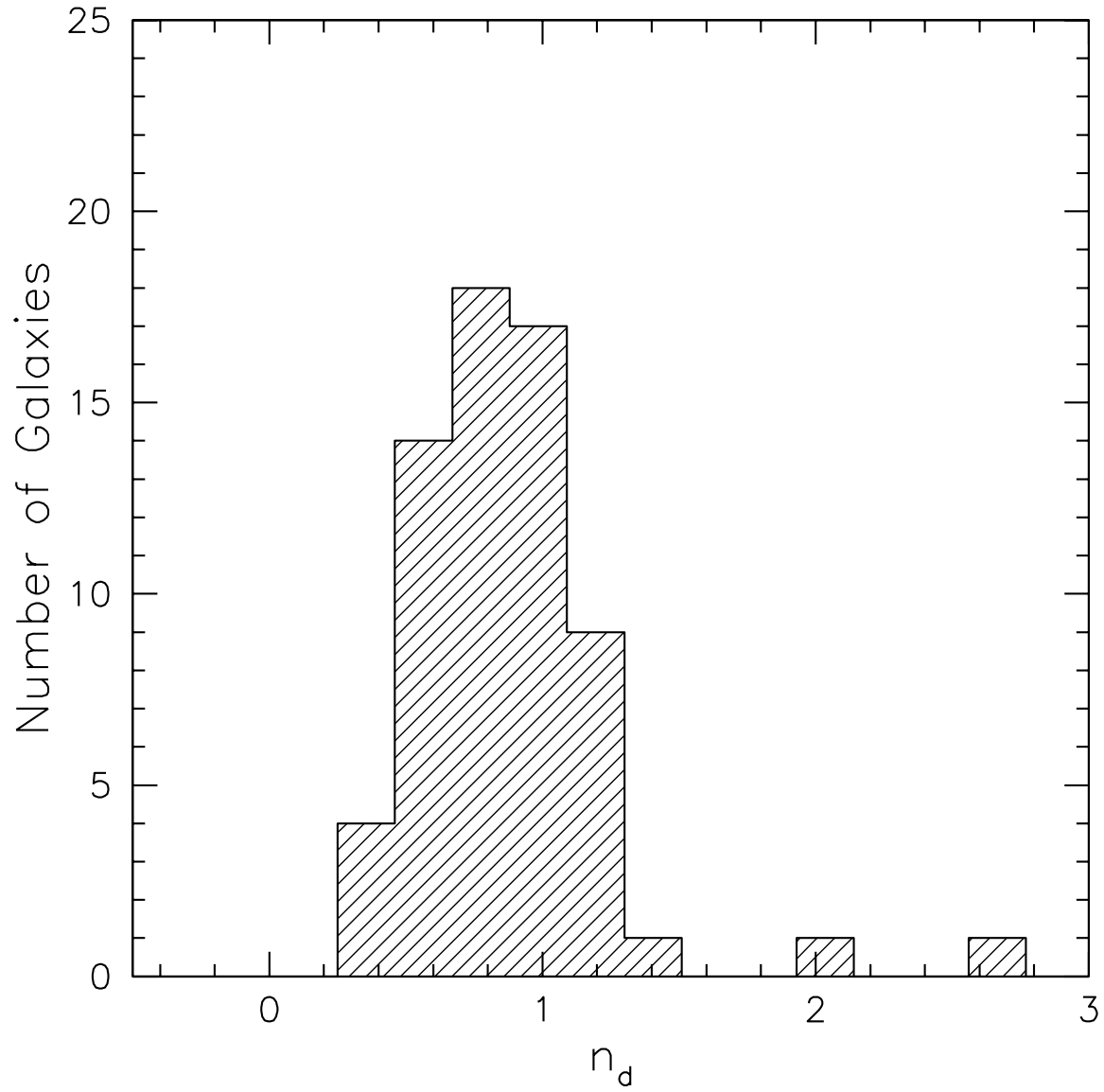


Figure 7. Distribution of Sérsic n parameters for the disks of the sample of 65 UMa galaxies computed from K' -band surface brightness profiles..

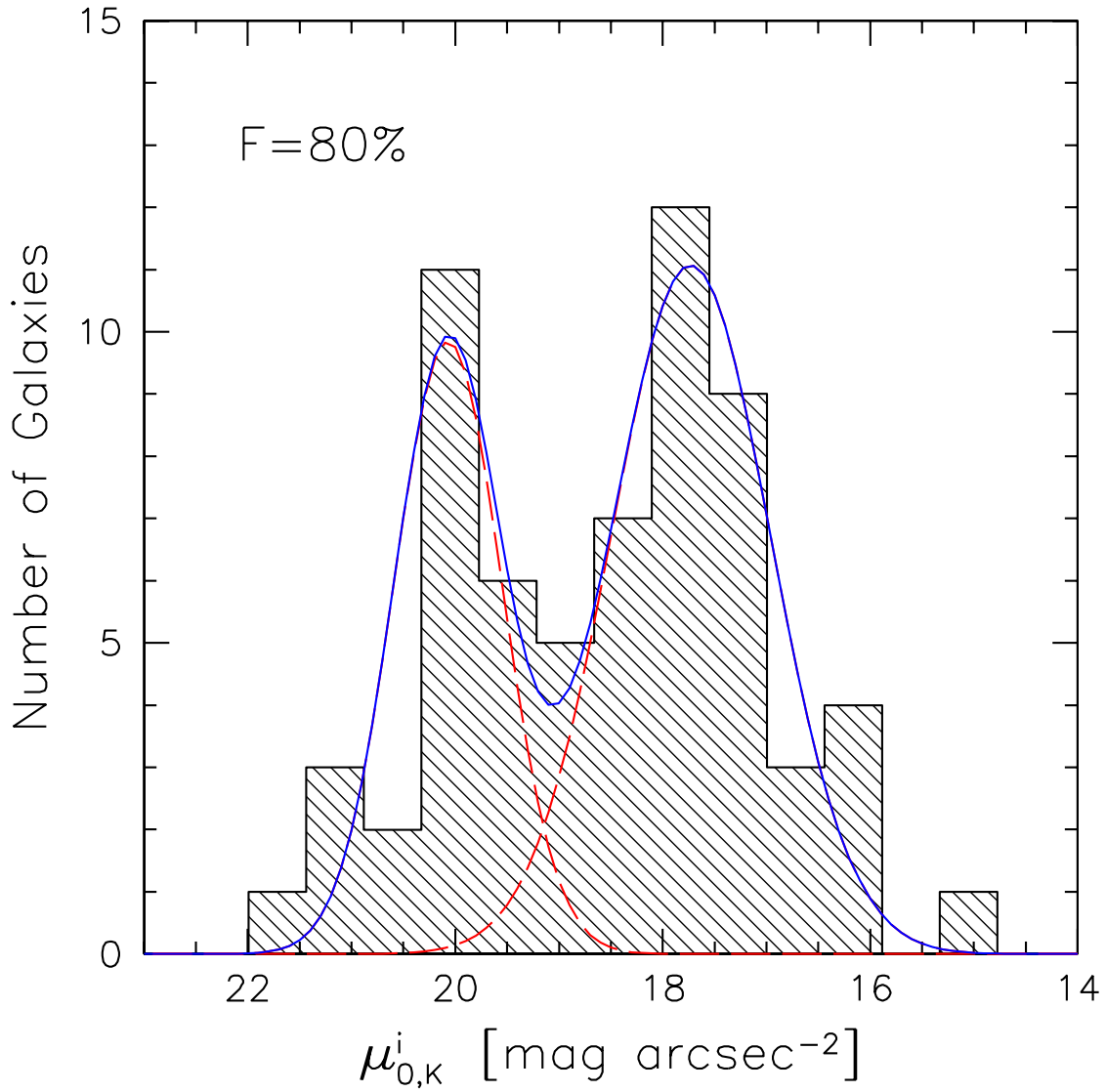


Figure 8. Distribution of inclination-corrected K' -band disk central surface brightnesses, $\mu_{0,K}^i$ for the sample of 65 UMa galaxies. The solid line represents the sum of the two Gaussian fits (dashed) to the histogram. The F-test confirms with 80% probability that this distribution for $\mu_{0,K}^i$ cannot be described by a Gaussian function.

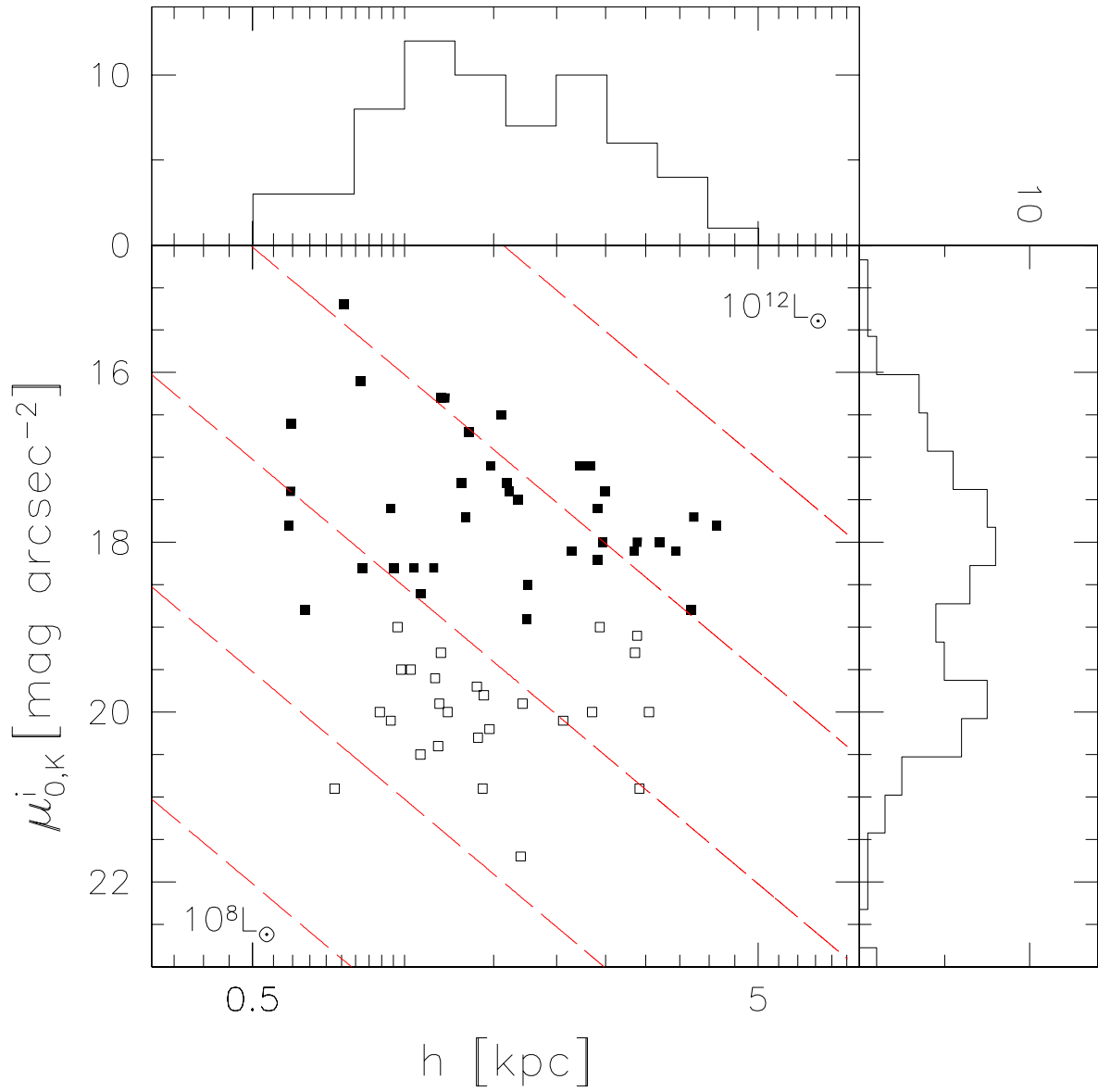


Figure 9. Distribution of inclination-corrected K' -band disk central surface brightnesses, $\mu_{0,K}^i$, as a function of disk scale length, h , measured in kpc (using a distance to UMa of 15.5 Mpc) for the sample of 65 UMa galaxies. The long-dashed lines represent lines of constant total disk luminosity while the different surface brightness classes are identified by open squares (LSB) and filled squares (HSB).

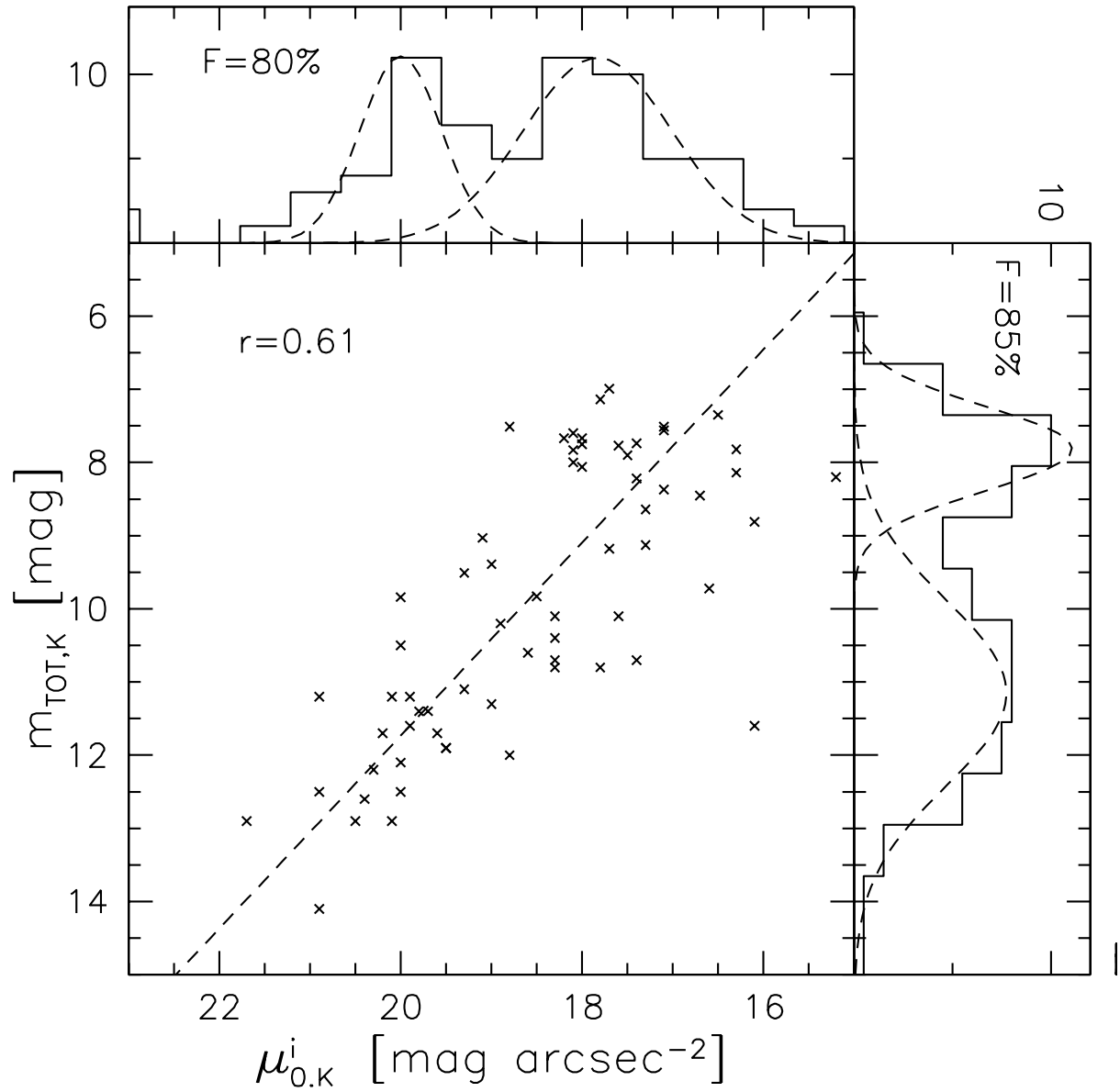


Figure 10. Distribution of inclination-corrected K' -band disk central surface brightnesses, $\mu_{0,K}^i$, as a function of total K' -band magnitude, m_{TOT}^K for the sample of 65 UMa galaxies. It is clear from the Pearson r coefficient of 0.61 that there is a correlation between $\mu_{0,K}^i$ and m_{TOT}^K .

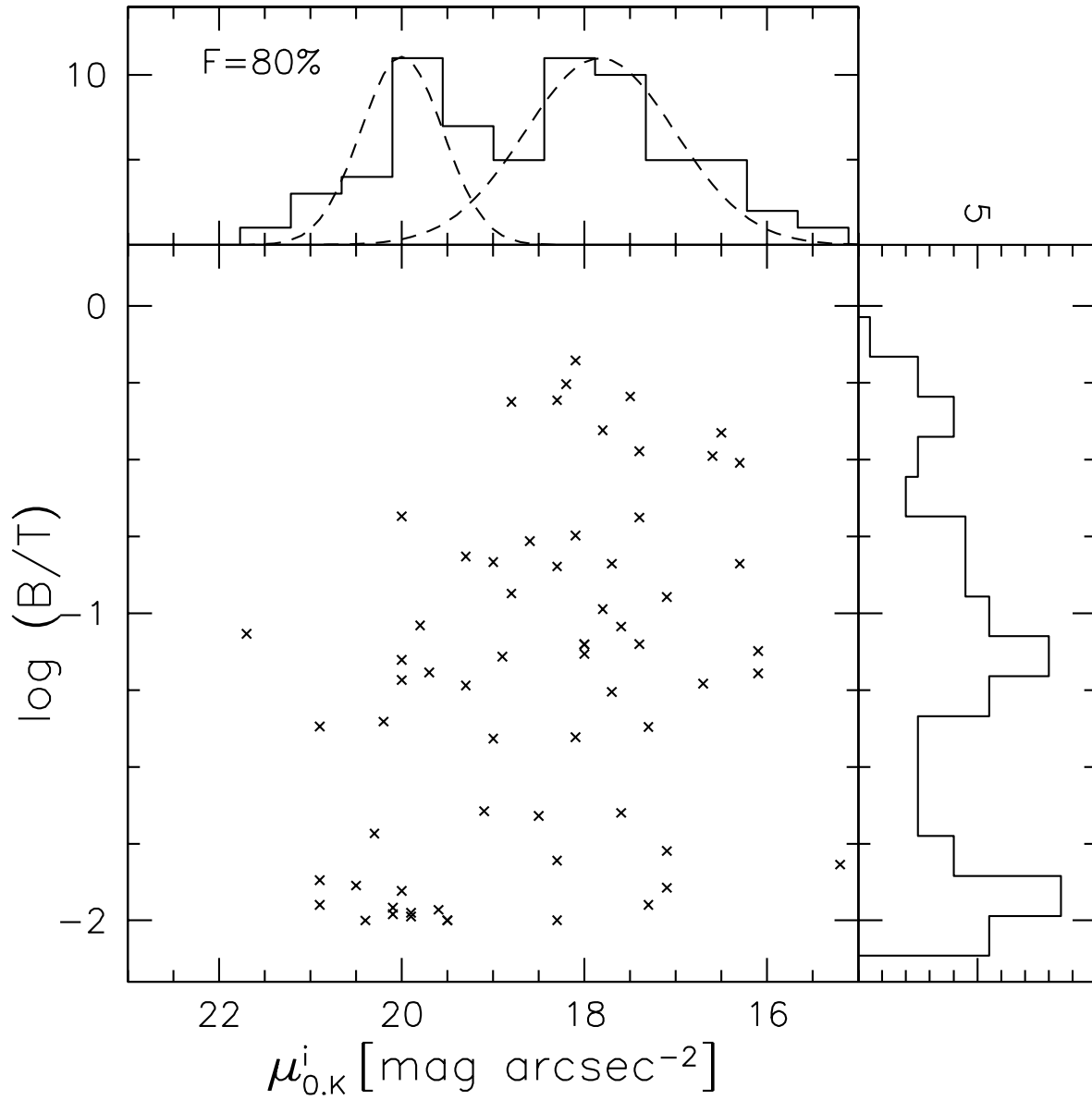


Figure 11. Distribution of inclination-corrected K' -band disk central surface brightnesses, $\mu_{0,K}^i$, as a function of bulge-to-total ratio, B/T , for the sample of 65 UMa galaxies.

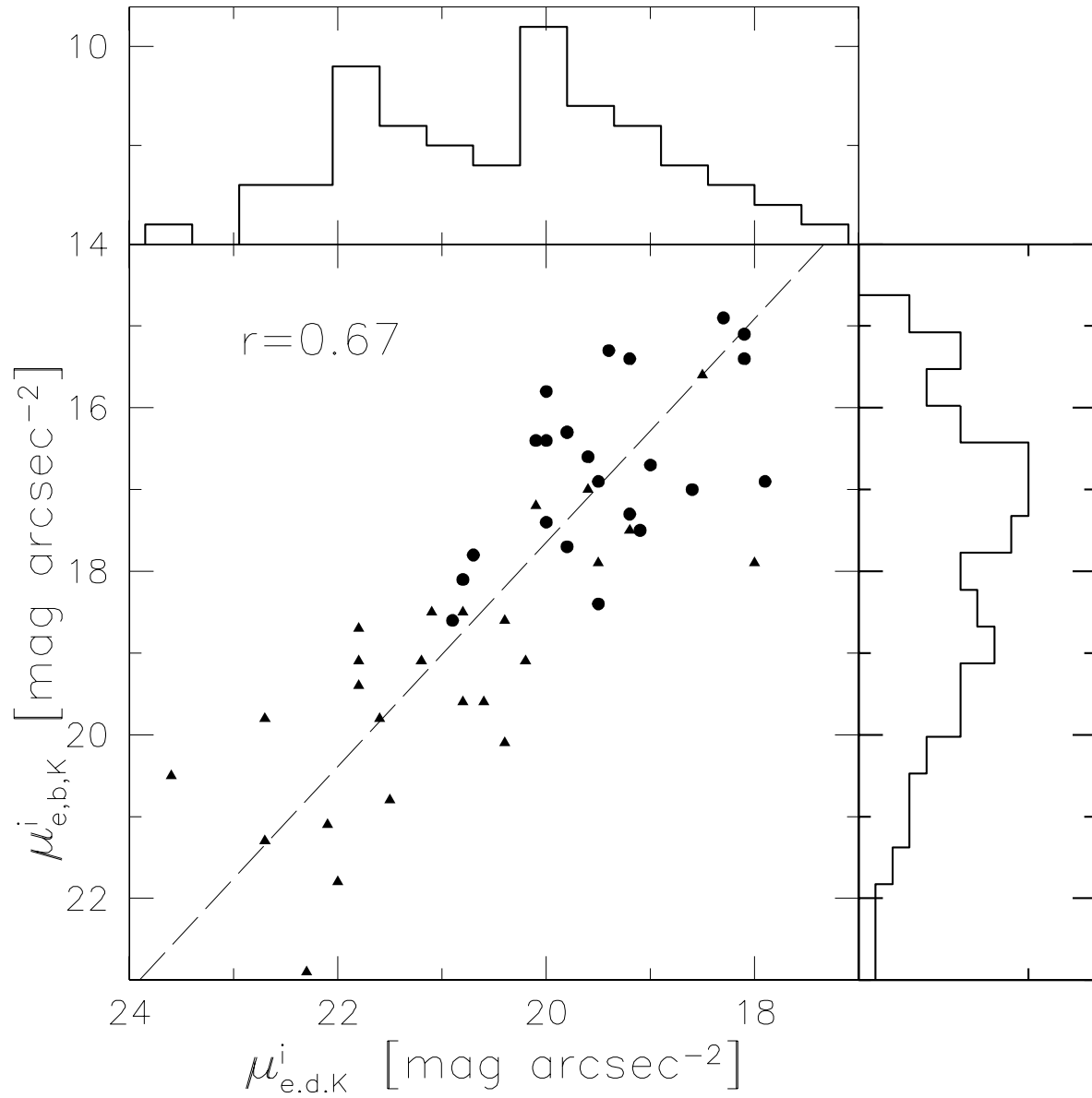


Figure 12. Distribution of inclination-corrected K' -band disk effective surface brightnesses, $\mu_{e,d}^i$, as a function of bulge effective surface brightness, $\mu_{e,b}$, for 48 UMa galaxies with discernible bulges. The circles refer to galaxies with $K'_{TOT} < 9.5$, while the triangles refer to galaxies fainter than this limit.

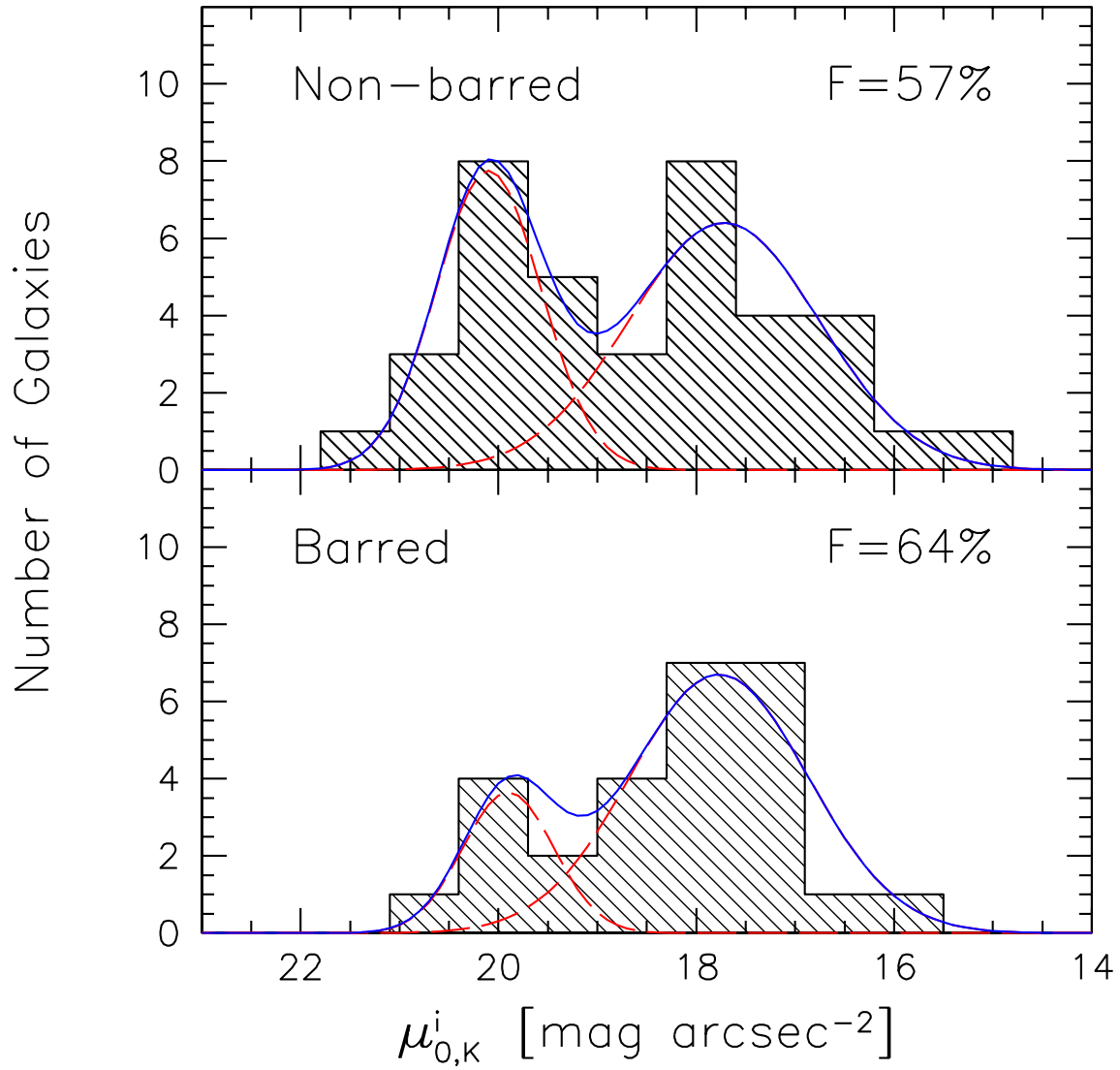


Figure 13. Distribution of inclination-corrected K' -band disk central surface brightnesses, μ_0^i for subsamples of barred and non-barred galaxies.

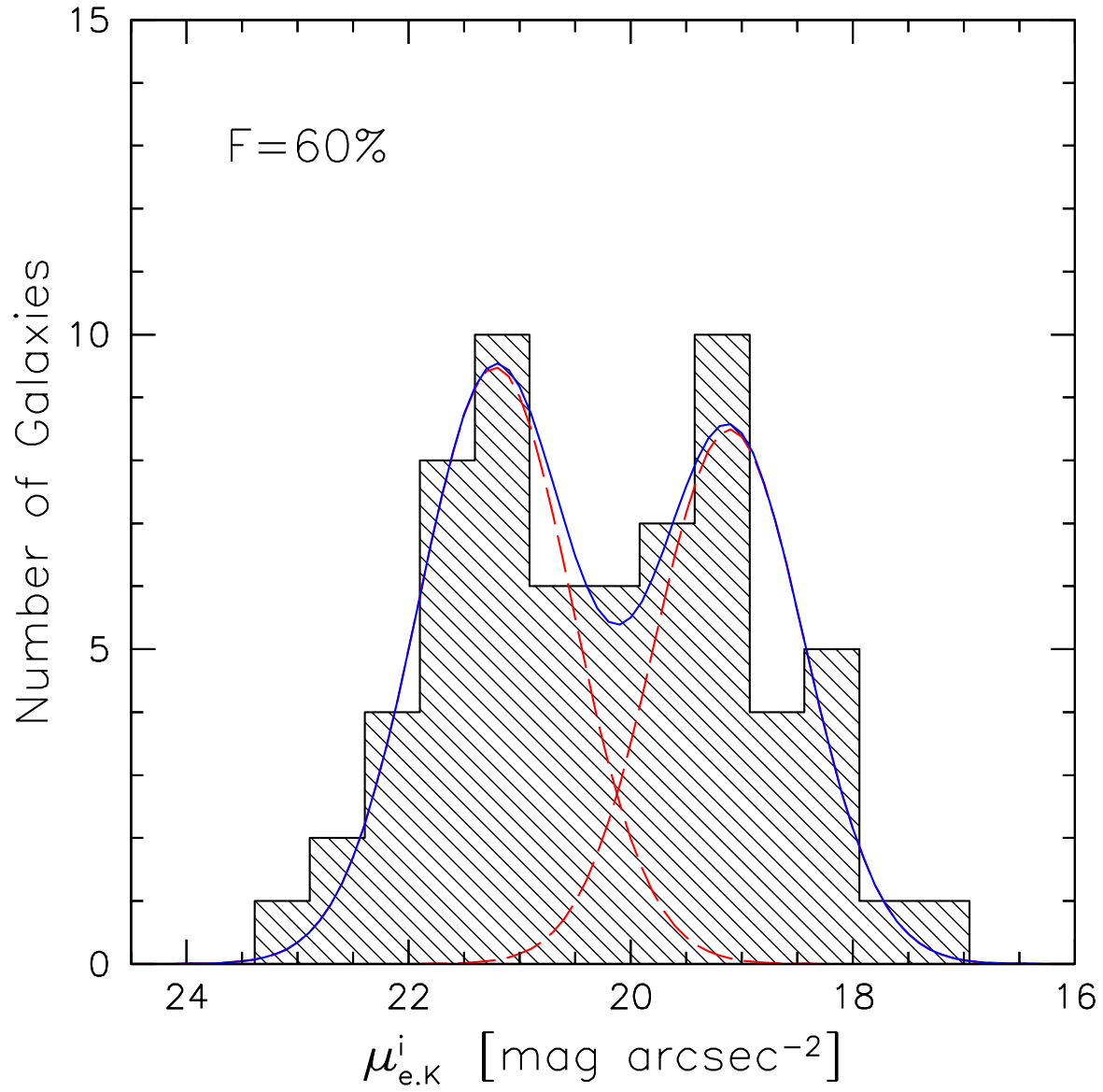


Figure 14. Distribution of inclination-corrected K' -band disk effective surface brightnesses, $\mu_{e,d}^i$ as measured by fitting the disk with a Sérsic function for the sample of 65 UMa galaxies. The solid line represents the sum of the two Gaussians (dashed lines).

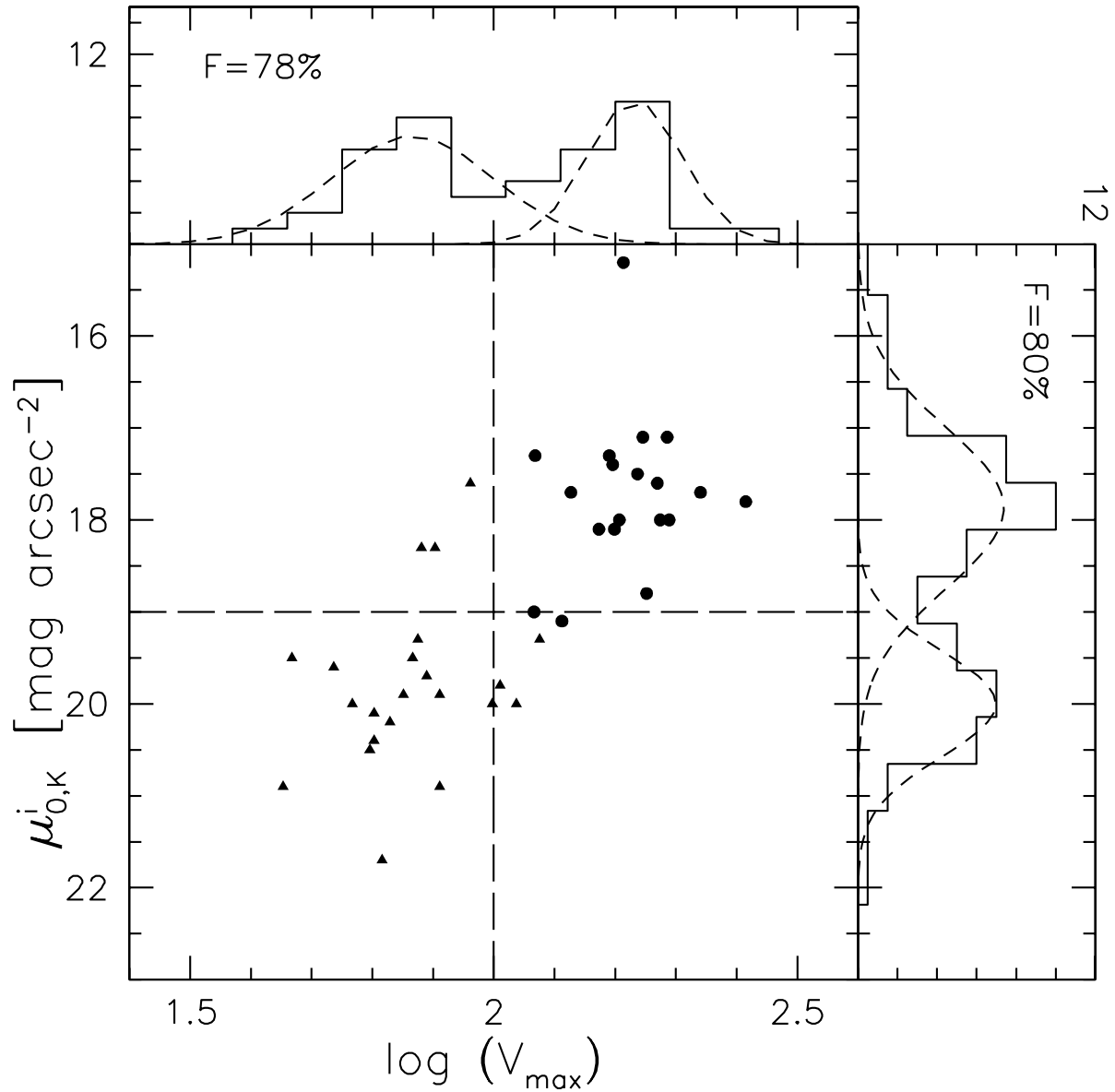


Figure 15. Distribution of inclination-corrected K' -band disk central surface brightnesses, $\mu_{0,K}^i$, as a function of the maximum rotational velocity, V_{max} , for 62 UMa galaxies with rotational velocities. The circles refer to galaxies with $K'_{TOT} < 9.5$ mag, while the triangles refer to galaxies fainter than this cutoff.